

Alignment of the CLAS12 central hybrid tracker with a Kalman Filter

S.J. Paul^{aq}, A. Peck^{aq}, M. Arratia^{aq,al}, Y. Gotra^{al}, V. Ziegler^{al}, R. De Vitaⁿ, F. Bossù^l, M. Defurne^l, H. Atac^{ak},
C. Ayerbe Gayoso^{at}, L. Baashenⁱ, N.A. Baltzell^{al}, L. Barion^l, M. Bashkanov^{as}, M. Battaglieriⁿ, I. Bedlinskiy^{aa},
B. Benkel^{am}, F. Benmokhtar^f, A. Bianconi^{ao,s}, L. Biondo^{n,o,p}, A.S. Biselli^g, M. Bondi^q, S. Boiarinov^{al},
K.-Th. Brinkmann^{af}, W.J. Briscoe^j, W.K. Brooks^{am}, D. Bulumulla^{ae}, V.D. Burkert^{al}, R. Capobianco^e,
D.S. Carman^{al}, J.C. Carvajalⁱ, P. Chatagnon^t, V. Chesnokov^{ai}, T. Chetry^{i,z,ad}, G. Ciullo^{l,h}, P.L. Cole^x,
G. Costantini^{ao,s}, A. D'Angelo^{q,ah}, N. Dashyan^{au}, A. Deur^{al}, S. Diehl^{af,e}, C. Djalali^{ad}, R. Dupre^t, A. El Alaoui^{am},
L. El Fassi^z, L. Elouadrhiri^{al}, A. Filippi^r, K. Gates^{ar}, G. Gavalian^{al}, Y. Ghandilyan^{au}, G.P. Gilfoyle^{ag},
A.A. Golubenko^{ai}, G. Gosta^{ao,s}, R.W. Gothe^{aj}, K. Griffioen^{at}, M. Guidal^t, H. Hakobyan^{am}, M. Hattawy^{ae},
F. Hauenstein^{al}, T.B. Hayward^{e,at}, D. Heddle^{d,al}, A. Hobart^t, M. Holtrop^{ab}, Y. Ilieva^{aj}, D.G. Ireland^{ar},
E.L. Isupov^{ai}, H.S. Jo^w, R. Johnston^y, K. Joo^e, D. Keller^l, M. Khachatryan^{ae}, A. Khanalⁱ, A. Kim^e, W. Kim^w,
V. Klimenko^e, A. Kripko^{af}, L. Lanza^q, M. Leali^{ao,s}, P. Lenisa^{l,h}, X. Li^y, I.J.D. MacGregor^{ar}, D. Marchand^t,
L. Marsicanoⁿ, V. Mascagna^{ao,s}, B. McKinnon^{ar}, C. McLauchlin^{aj}, S. Migliorati^{ao,s}, T. Mineeva^{am}, M. Mirazita^m,
V. Mokeev^{al}, C. Munoz Camacho^t, P. Nadel-Turonski^{al}, P. Naidoo^{ar}, K. Neupane^{aj}, D. Nguyen^{al}, S. Niccolai^t,
M. Nicol^{as}, G. Niculescu^v, M. Osipenkoⁿ, P. Pandey^{ae}, M. Paolone^{ac,ak}, R. Paremuzyan^{al,ab}, N. Pilleux^t,
O. Pogorelko^{aa}, M. Pokhrel^{ae}, J. Poudel^{ae}, J.W. Price^a, Y. Prok^{ae}, T. Reedⁱ, M. Ripaniⁿ, J. Ritman^{k,u}, F. Sabatié^c,
S. Schadmand^k, A. Schmidt^{j,y}, E.V. Shirokov^{ai}, U. Shrestha^{e,ad}, P. Simmerling^e, M. Spreafico^{ap,n}, D. Sokhan^{e,ar},
N. Sparveris^{ak}, I.I. Strakovsky^j, S. Strauch^{aj}, J.A. Tan^w, R. Tyson^{ar}, M. Ungaro^{al}, S. Vallarino^l, L. Venturelli^{ao,s},
H. Voskanyan^{au}, E. Voutier^t, D.P. Watts^{as}, X. Wei^{al}, R. Wishart^{ar}, M.H. Wood^b, N. Zachariou^{as}

^aCalifornia State University, Dominguez Hills, Carson, CA 90747

^bCanisius College, Buffalo, NY

^cIRFU, CEA, Université Paris-Saclay, F-91191 Gif-sur-Yvette, France

^dChristopher Newport University, Newport News, Virginia 23606

^eUniversity of Connecticut, Storrs, Connecticut 06269

^fDuquesne University, Pittsburgh, PA 15282 USA

^gFairfield University, Fairfield CT 06824

^hUniversità di Ferrara, 44121 Ferrara, Italy

ⁱFlorida International University, Miami, Florida 33199

^jThe George Washington University, Washington, DC 20052

^kGSI Helmholtzzentrum für Schwerionenforschung GmbH, D-64291 Darmstadt, Germany

^lINFN, Sezione di Ferrara, 44100 Ferrara, Italy

^mINFN, Laboratori Nazionali di Frascati, 00044 Frascati, Italy

ⁿINFN, Sezione di Genova, 16146 Genova, Italy

^oINFN, Sezione di Catania, 95123 Catania, Italy

^pUniversità degli Studi di Messina, 98166 Messina, Italy

^qINFN, Sezione di Roma Tor Vergata, 00133 Rome, Italy

^rINFN, Sezione di Torino, 10125 Torino, Italy

^sINFN, Sezione di Pavia, 27100 Pavia, Italy

^tUniversité Paris-Saclay, CNRS/IN2P3, IJCLab, 91405 Orsay, France

^uInstitute für Kernphysik (Juelich), Juelich, Germany

^vJames Madison University, Harrisonburg, Virginia 22807

^wKyungpook National University, Daegu 41566, Republic of Korea

^xLamar University, 4400 MLK Blvd, PO Box 10046, Beaumont, Texas 77710

^yMassachusetts Institute of Technology, Cambridge, Massachusetts 02139-4307

^zMississippi State University, Mississippi State, MS 39762-5167

^{aa}National Research Centre Kurchatov Institute - ITEP, Moscow, 117259, Russia

^{ab}University of New Hampshire, Durham, New Hampshire 03824-3568

^{ac}New Mexico State University, PO Box 30001, Las Cruces, NM 88003, USA

^{ad}Ohio University, Athens, Ohio 45701

^{ae}Old Dominion University, Norfolk, Virginia 23529

^{af}III Physikalisches Institut der Universität Giessen, 35392 Giessen, Germany

URL: miguel.arratia@ucr.edu (M. Arratia)

52 *^{ag}University of Richmond, Richmond, Virginia 23173*
53 *^{ah}universit  di Roma Tor Vergata, 00133 Rome Italy*
54 *^{ai}Skobeltsyn Institute of Nuclear Physics, Lomonosov Moscow State University, 119234 Moscow, Russia*
55 *^{aj}University of South Carolina, Columbia, South Carolina 29208*
56 *^{ak}Temple University, Philadelphia, PA 19122*
57 *^{al}Thomas Jefferson National Accelerator Facility (Jefferson Lab), Newport News, Virginia 23606*
58 *^{am}Universidad T cnica Federico Santa Mar a, Casilla 110-V Valpara so, Chile*
59 *^{an}Universit  degli Studi dell'Insubria, 22100 Como, Italy*
60 *^{ao}Universit  degli Studi di Brescia, 25123 Brescia, Italy*
61 *^{ap}Universit  di Genova, Dipartimento di Fisica, 16146 Genova, Italy*
62 *^{aq}University of California Riverside, 900 University Avenue, Riverside, CA 92521, USA*
63 *^{ar}University of Glasgow, Glasgow G12 8QQ, United Kingdom*
64 *^{as}University of York, York YO10 5DD, United Kingdom*
65 *^{at}College of William and Mary, Williamsburg, Virginia 23187-8795*
66 *^{au}Yerevan Physics Institute, 375036 Yerevan, Armenia*

67 **Abstract**

68 Several factors can contribute to the difficulty of aligning the sensors of tracking detectors, including a large number of
69 modules, multiple types of detector technologies, and non-linear strip patterns on the sensors. All three of these factors
70 apply to the CLAS12 CVT, which is a hybrid detector consisting of planar silicon sensors with non-parallel strips, and
71 cylindrical micromegas sensors with longitudinal and arc-shaped strips located within a 5 T superconducting solenoid.

72 To align this detector, we used the Kalman Alignment Algorithm, which accounts for correlations between the
73 alignment parameters without requiring the time-consuming inversion of large matrices. This is the first time that
74 this algorithm has been adapted for use with hybrid technologies, non-parallel strips, and curved sensors.

We present the results for the first alignment of the CLAS12 CVT using straight tracks from cosmic rays and from
a target with the magnetic field turned off. After running this procedure, we achieved alignment at the level of 10 μm ,
and the widths of the residual spectra were greatly reduced. These results attest to the flexibility of this algorithm
and its applicability to future use in the CLAS12 CVT and other hybrid or curved trackers, such as those proposed
for the future Electron-Ion Collider.

1. Introduction

Aligning a tracking detector is a non-trivial task, which can involve large numbers of degrees of freedom. Various algorithms have been developed for this task, such as HIP [1] and MillePede [2]. The Kalman Alignment Algorithm (KAA) [3, 4], which is based on the Kalman-filter algorithm, was first implemented to align the CMS silicon tracker [5], and we use it to align the CEBAF Large Acceptance Spectrometer (CLAS12) Central Vertex Tracker (CVT) [6–8] in Hall B at Jefferson Lab.

These algorithms take the fitted tracks, reconstructed from misaligned detector data, and a model of the dependence of the residuals of the track fit to the alignment and track parameters. Here, the residuals are the differences between the measurements along the track and the values interpolated from the track fit. The goal of these algorithms is then to find the values of the alignment parameters that minimize the sum of squares of the residuals (*i.e.* the track fit χ^2).

When choosing an alignment algorithm, two important factors are the computational speed and biases in the results. One drawback to the MillePede algorithm is that it requires the inversion of a large matrix, typically of rank $N_{\text{align}} \times N_{\text{align}}$, where N_{align} is the number of alignment parameters, which can be time-consuming. The Hits and Impact Points (HIP) algorithm is similar to MillePede, except that it forces the analogous matrix to be block-diagonal (and thus much faster to invert) at the cost of ignoring the dependence of the residuals on the track parameters (which MillePede and the KAA take into account). Because this dependence is ignored, the correlations between alignment parameters for one module and those of another module are not accounted for and can introduce biases in the results. The KAA overcomes both of these problems. Like MillePede, it corrects for the biases caused by the track-parameter dependence of the residuals, but the KAA does so in a manner that avoids the inversion of large matrices.

The results obtained with the HIP, KAA, and MillePede algorithms for the CMS inner tracker were compared to one another in Ref. [5]. The tracking-residual distributions obtained with the three algorithms were all centered within a few μm of zero and had comparable RMS values to one another (about $300 \mu\text{m}$).

One important difference between CMS and the CLAS12 CVT is that the strips in the sensors in CMS are straight

and parallel¹, whereas the CLAS12 CVT has both non-parallel strips within the same sensor and sensors that are curved. These two features cause the tracking residuals to depend non-linearly on the alignment parameters. The HIP, KAA, and Millepede algorithms all approximate the relationship between these residuals and the alignment parameters as linear, causing such algorithms to converge at non-optimal values for the alignment parameters.

A solution to this issue was used for the LHCb VELO (silicon VERtEx LOcator), which consists of silicon sensors with azimuthally curved and radial strips rigidly mounted on half-disks [9]. To determine the relative alignment of the radial and azimuthal sensors, they used multiple iterations of a fast, specialized algorithm that is similar to HIP, and refitted the tracks between iterations with the alignment parameters obtained from the previous iteration [10]. From this, they obtained an alignment precision on the level of $1.3 \mu\text{m}$ between the radial and azimuthal sensors of each half disk.

In this work, we use the KAA to align the CLAS12 CVT using a multiple-iteration approach similar to Ref. [10]. The CLAS12 CVT presents two new challenges for the KAA that were not applicable when it was first implemented for CMS: the CVT is a hybrid of two different types of sensor technology, silicon and micromegas, while CMS is a fully silicon tracker, and the CVT includes curved sensors, while the sensors at CMS are flat. Thus, the alignment of the CVT using the KAA is a test of the versatility and flexibility of the algorithm for diverse detectors.

Details of the CLAS12 CVT are given in Sec. 2. We then describe the KAA in Sec. 3. Section 4 describes the datasets used for alignment. In Sec. 5, we describe the procedure for running the KAA for the CLAS12 CVT. We then present the results for the data in Sec. 6 and we conclude in Sec. 7.

2. The CLAS12 Central Vertex Tracker

The CLAS12 CVT, which covers the polar-angle² range $35^\circ < \theta < 125^\circ$, is shown in Fig. 1. It consists of three regions of double-sided Silicon Vertex Tracker (SVT) modules [7] and six layers of the Barrel Micromegas Tracker

¹The strips in one sensor of CMS are not necessarily parallel to those in another sensor, since there is a stereo angle between nearby sensors.

²Throughout this paper, the lab-frame coordinates are defined as follows: z is along the beam direction, y is the up direction, and x is to the left when looking at the detector from upstream.

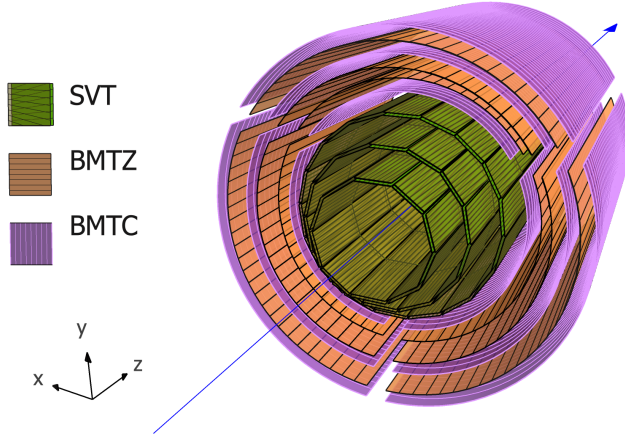


Figure 1: Rendering of the CLAS12 CVT, which consists of three double layers of SVT (inner, leaf-green) and six layers of BMT, with Z layers in orange and C layers in purple. The blue line represents the beamline. The lines within the sensors indicate every 32nd strip.

162 (BMT) [8].

163 The SVT regions are arranged in concentric polygons
 164 with 10, 14, and 18 sectors in the inner, middle, and outer
 165 pairs of layers³. The geometry of the SVT is summarized
 166 in Table 1. Within each pair of layers, each sector is a
 167 separate module, consisting of one sensor on each of the
 168 two layers, separated radially by 3.162 mm. The sensor
 169 consists of three daisy-chained silicon microstrip detec-
 170 tors and has 256 strips. Each detector is $320\ \mu\text{m}$ thick,
 171 42.00 mm wide, and 111.63 mm long. A rendering of the
 172 geometry of the SVT module is shown in Fig. 2.

173 At the upstream end of the sensor planes, where the
 174 strips connect to the readout, they have $156\ \mu\text{m}$ pitch, but
 175 they fan out, with the angle of the strip relative to longi-
 176 tudinal direction of the sensor increasing linearly from 0°
 177 at the first strip to 3° at the last strip. The two sensors
 178 in each module are mounted back-to-back, so that the first
 179 strip of one sensor corresponds with the last strip of the
 180 other and vice versa. This geometry allows measurements
 181 of the longitudinal hit positions due to the 3° stereo angle
 182 between the two sensors on each module.

183 The BMT is divided azimuthally into three sectors,
 184 each of which consists of six cylindrical arc layers. There
 185 are two types of sensors: Z-type (layers 2, 3, and 5), in

³Since the pairs of layers have different numbers of modules, the sectors in one double layer do not line up with those in the other double layers, with the exception of the top and bottom sector in each double layer.

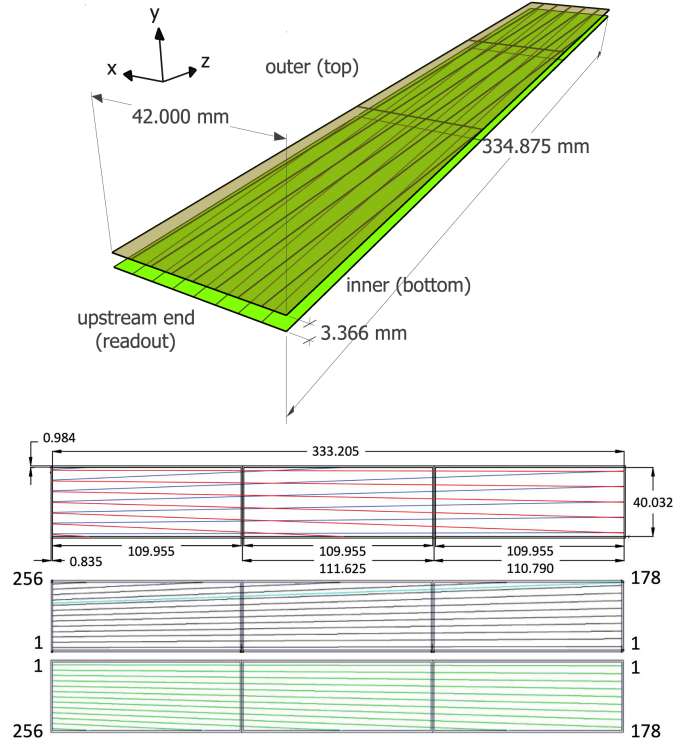


Figure 2: Top: 3D Rendering of one of the SVT sector modules. The inner (outer) sensor of the module is shown in green (yellow). Every 32nd strip is shown for both sensors as lines on the sensors. Bottom (from Ref. [7]): Sensor strip layout. The upstream end, which has the readout, is on the left side. Strip numbers are indicated. Dimensions are in mm.

Layer	Radius (mm)	Pitch (μm)	Sectors
1	65.29	156-224	10
2	68.77	156-224	10
3	92.89	156-224	14
4	96.37	156-224	14
5	120.32	156-224	18
6	123.80	156-224	18

Table 1: Summary of parameters of each SVT layer. The radii given are the nominal values for the perpendicular distance between the midplane of the SVT backing structure and the beamline. The pitch varies from $156\ \mu\text{m}$ at the upstream end to about $224\ \mu\text{m}$ at the downstream end.

Layer	Radius (mm)	Pitch (μm)	Strip orientation
1	146.15	330–860	C
2	161.15	487	Z
3	176.15	536	Z
4	191.15	340–770	C
5	206.15	529	Z
6	221.15	330–670	C

Table 2: Summary of parameters of each BMT layer. The pitches of the C layers vary from strip to strip, with wider strips towards the front and back, and narrower strips near the center.

which the strips are (nominally) parallel to the beamline and measure the azimuthal position of the particle’s trajectory, and C-type (layers 1, 4, and 6) in which the strips curve azimuthally around the beamline and measure the longitudinal position of the particle’s trajectory (which is also used to measure the polar angle of the trajectory). Throughout this paper, we refer to the Z layers as the BMTZ and the C layers as the BMTZ. The radii, pitches, and strip orientations for each layer are given in Table 2.

3. Methodology

We used the KAA, which is described in detail in Refs. [3, 4]. Here we present a summary of the main features of the algorithm and detail the specific implementation to the CLAS12 case. We note here that our method relies on straight tracks to obtain the alignment parameters and was validated with both straight and curved tracks.

A Kalman filter is an algorithm that uses an ordered sequence of measurements and produces estimates of unknown parameters that converge upon more precise values than those obtained from a single measurement. Like any other Kalman-filter algorithm, the KAA begins with an estimate of the parameters to be fitted and a matrix of the covariances among these parameters. It then loops through the measurements in the input sample and updates the values of the parameters and their covariance matrix after each measurement. In the case of the KAA, the parameters to be fitted are the alignment parameters, and the measurements are fitted tracks and the tracking residuals thereof⁴. As more tracks are processed, the uncertainties on the alignment parameters (that is, the square roots of the diagonal elements of the covariance

⁴This is analogous to the Kalman-filter track-fitting algorithm, where the parameters of a single track are fitted, and the individual measurements are the hits and/or clusters along the track.

matrix) decrease, and the alignment parameters converge to more precise values.

In the KAA, the deviations of each sensor and module from their nominal positions are represented by the column vector \mathbf{d} . The KAA requires a preliminary estimate of \mathbf{d} and its covariance matrix \mathbf{D} , and a set of several matrices for each track. These matrices, which are summarized below, model the track residuals for each measurement in the track, their dependence on the alignment and track parameters, and the expected resolution on these residuals and are summarized below. The alignment values and its covariance matrix are updated sequentially for every track in the sample of input events.

Straight-line tracks in the CVT are represented by their direction, \hat{u} , and a point on the line, \vec{x}_{ref} . Unless otherwise noted, all coordinates are given in the lab frame. We use the following track parameters: the distance of closest approach of the track to the beamline, d_0 , the azimuthal angle of the track direction, ϕ_0 , the longitudinal position of the track’s point of closest approach, z_0 , and the tangent of the track’s dip angle, t_0 . Expressed in terms of these parameters, \vec{x}_{ref} and \hat{u} are:

$$\vec{x}_{\text{ref}} = (-d_0 \sin \phi_0 + x_b, d_0 \cos \phi_0 + y_b, z_0) \quad (1)$$

and

$$\hat{u} = \frac{(\cos \phi_0, \sin \phi_0, t_0)}{\sqrt{1 + t_0^2}}, \quad (2)$$

where (x_b, y_b) is the beam position.

In the CVT, each measurement corresponds to a contiguous cluster of hits in one of the SVT or BMT layers. We represented these clusters as line segments connecting the centroids⁵ of the endpoints of the strips on one end of the sensor to the centroid of the endpoints of the strips on the other end. Notice the direction of each line segment in the lab frame is not necessarily parallel to a particular strip. We defined the vector \vec{e} to be the coordinates (in the lab frame) of a point on this line segment (arbitrarily, we chose the midpoint), and $\hat{\ell}$ to be the direction of this line, *i.e.*, the direction of the lines connecting the centroids of the endpoints of the strips on each end of the sensor⁶. We also defined the unit vector \hat{n} as the unit normal vector to the sensor, and $\hat{s} = \hat{n} \times \hat{\ell}$, which we call the “measurement direction”, as shown in Fig. 3.

⁵weighted by the reconstructed energy deposited in the strip

⁶For the SVT, which has non-parallel strips, this is the weighted average of the directions of the strips in the cluster

256 For the BMTC, each strip is an arc, therefore we anal-231
 257 ogously constructed a ‘‘centroid’’ arc using the centroids232
 258 of two endpoints and centers of the individual strip’s arcs233
 259 We then extrapolated the track to the BMTC layer, and234
 260 find the line that is tangent to the arc at the same az-235
 261 imuthal position as the extrapolation point (right pane236
 262 of Fig. 3). The vectors \vec{e} and $\hat{\ell}$ are then defined as a point237
 263 on this line (we chose the tangent point) and the direction238
 264 of the line respectively. The measurement direction, \hat{s} , is239
 265 defined to be along the BMTC layer’s cylindrical axis, and240
 266 \hat{n} is normal to the sensor at the extrapolated azimuthal241
 267 position.242

268 Using these representations of the track and its clus-243
 269 ters, we then determined the matrices needed for the244
 270 KAA’s input. The first two matrices are a column vecto245
 271 of the 1D measurements along the track, \mathbf{m} , and another246
 272 column vector \mathbf{c} of the expected values for each measure-247
 273 ment based on a track fit performed in reconstruction,
 274 which is made using the the Kalman Filter algorithm [11],248
 275 The tracking-residuals column vector, \mathbf{r} , is defined as their249
 276 difference, $\mathbf{m} - \mathbf{c}$.250

251 We calculated the element of the column vectors \mathbf{c} ,252
 253 \mathbf{m} , and \mathbf{r} corresponding to the i^{th} measurement along the254
 255 track using the following formulas:

$$256 \quad c_i = \hat{s} \cdot \left(\vec{x}_{\text{ref}} + \hat{u} \frac{\hat{n} \cdot (\vec{e} - \vec{x}_{\text{ref}})}{\hat{u} \cdot \hat{n}} \right), \quad (3)$$

$$257 \quad m_i = \hat{s} \cdot \vec{e}, \quad (4)$$

258 and

$$259 \quad r_i = m_i - c_i, \quad (5)$$

$$260 \quad = \hat{s} \cdot \left(\vec{e} - \vec{x}_{\text{ref}} - \hat{u} \frac{\hat{n} \cdot (\vec{e} - \vec{x}_{\text{ref}})}{\hat{u} \cdot \hat{n}} \right) \quad (6)$$

$$261 \quad = \vec{s}' \cdot (\vec{e} - \vec{x}_{\text{ref}}), \quad (7)$$

262 where

$$263 \quad \vec{s}' = \hat{s} - \frac{\hat{s} \cdot \hat{u}}{\hat{u} \cdot \hat{n}} \hat{n}. \quad (8)$$

264 Eq. 7 is equivalent to the distance along the measurement
 265 direction, \hat{s} , between the centroid line of the cluster of
 266 hits on the sensor and the extrapolated position where
 267 the track intersects the sensor.
 268

269 The next matrix in the input, \mathbf{V} , represents the stochas-
 270 tic part of the measurement. The elements of \mathbf{V} can be
 271 expressed as the expectation value of the product of the
 272 residuals for two (not necessarily distinct) measurements
 273 in a track,
 274

$$275 \quad V_{ij} = \langle r_i r_j \rangle, \quad (9)$$

276 where i and j are the indices of the two measurements
 277 within the track.

278 In models where the residuals in one sensor are uncor-
 279 related with those in the other sensors (as is assumed in
 280 this work), this matrix is diagonal, where each element is
 281 the square of the resolution for the corresponding mea-
 282 surement in the track. We used the spacial resolutions
 283 that are calculated in the CLAS12 reconstruction pack-
 284 age [12]. For the SVT, where the strips get wider further
 285 downstream, the width is calculated at the longitudinal
 286 position of the intersection of the clusters in a stereo pair.

287 The dependence of the residuals on the alignment pa-
 288 rameters and on the track parameters are modeled lin-
 289 early by the alignment-derivative matrix, \mathbf{A} , and the track-
 290 derivative matrix \mathbf{B} . The elements of \mathbf{A} are defined by

$$291 \quad A_{ij} = \frac{\partial r_i}{\partial x_j}, \quad (10)$$

292 where r_i is the residual of the i^{th} measurement in the track
 293 and x_j is the j^{th} alignment parameter. In this work, we
 294 assume that every module is a rigid body, and therefore
 295 consider only rotation and translation, but not deforma-
 296 tions within any module. For three rotation variables and
 297 three translation variables per module, \mathbf{A} has dimension
 298 $n_{\text{meas}} \times 6n_{\text{mod}}$, where n_{meas} is the number of measure-
 299 ments (clusters) in the track, and n_{mod} is the total num-
 300 ber of modules to be aligned.

301 The elements of \mathbf{B} are likewise defined as

$$302 \quad B_{ij} = \frac{\partial r_i}{\partial t_j}, \quad (11)$$

303 where r_i is the residual of the i^{th} measurement in the track
 304 and t_j is the j^{th} track parameter. Since four parameters
 305 define a straight track, \mathbf{B} has dimension $n_{\text{meas}} \times 4$.

306 In our implementation, the elements of the alignment-
 307 derivative matrix, \mathbf{A} , are

$$308 \quad A_{i,\vec{T}} = \vec{s}' \quad (12)$$

309 and

$$310 \quad A_{i,\vec{R}} = -\vec{s}' \times \left(\vec{x}_{\text{ref}} + \left(\frac{\vec{n} \cdot (\vec{e} - \vec{x}_{\text{ref}})}{\hat{u} \cdot \hat{n}} \right) \hat{u} \right). \quad (13)$$

311 The \vec{T} and \vec{R} vectors represent the groups of indices cor-
 312 responding to the translation and rotation parameters of
 313 the module which the i^{th} measurement in the track takes
 314 place in.

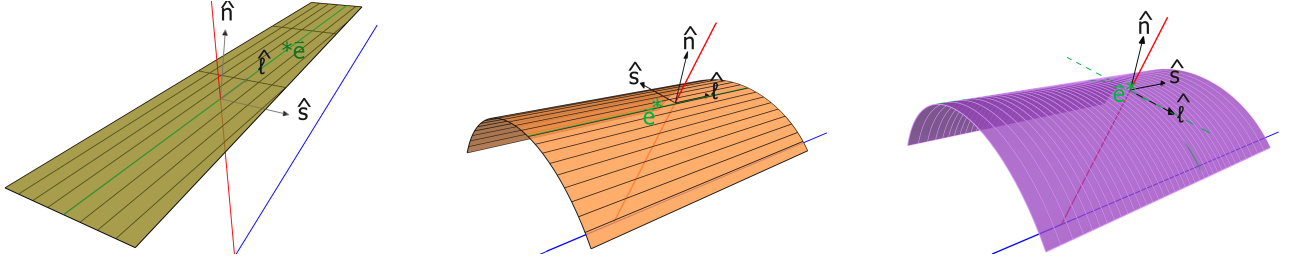


Figure 3: Illustrations of the vectors \hat{s} , \hat{n} , and $\hat{\ell}$ for the SVT (left), BMTZ (middle), and BMTC (right). The beamline and the reference trajectory are shown in blue and red, respectively. The struck strip is shown as a solid green line or arc. For the BMTC, the tangent line to the struck strip is shown as a green dashed line. A point on the line, \vec{e} , is indicated by an asterisk (for the SVT and BMTZ, we chose one of the endpoints of the strip; for the BMTC, we used the tangent point).

The elements of the track-derivative matrix, \mathbf{B} , are and

$$B_{i,d_0} = -\vec{s}' \cdot (-\sin \phi_0, \cos \phi_0, 0) \quad (14)$$

$$B_{i,\phi_0} = -\vec{s}' \cdot \left(\frac{\hat{n} \cdot (\vec{e} - \vec{x}_{\text{ref}})}{\hat{u} \cdot \hat{n} \sqrt{1 + t_0^2}} (-\sin \phi_0, \cos \phi_0, 0) \right. \\ \left. - d_0 (\cos \phi_0, \sin \phi_0, 0) \right) \quad (15)$$

$$B_{i,z_0} = -s'_z \quad (16)$$

$$B_{i,t_0} = -s'_z \frac{\hat{n} \cdot (\vec{e} - \vec{x}_{\text{ref}})}{\hat{u} \cdot \hat{n}}. \quad (17)$$

Equation 12 was obtained by taking the derivative of the formula for the residuals (Eq. 7) with respect to \vec{e} . To obtain Eq. 13, we took the derivative of Eq. 7 with respect to an infinitesimal rotation $d\vec{R}$ of the sensor: $\hat{n} + d\vec{R} \times \hat{n}$, and likewise for \hat{s} , $\hat{\ell}$, and \vec{e} . The track is not rotated, so the vectors \hat{u} and \vec{x}_{ref} are not rotated.

Eqs. 14-17 were obtained by taking the derivative of Eq. 7 with respect to the track parameters d_0 , ϕ_0 , z_0 , and t_0 , using the definitions of \vec{x}_{ref} and \hat{u} in Eqs. 1 and 2.

The degrees of freedom corresponding to the matrix elements of \mathbf{A} and \mathbf{B} are illustrated in Figs. 4, 5, and 6 for the SVT, BMTZ, and BMTC, respectively.

Following Refs. [3, 4], KAA loops through all of the tracks, and updates \mathbf{d} and \mathbf{D} using Eqs. 18-21 below (the derivations of these equations are beyond the scope of this article, and can be found in Refs. [3, 4]):

$$\mathbf{d}' = \mathbf{d} + \mathbf{D}\mathbf{A}^T\mathbf{G}(\mathbf{m} - \mathbf{c} - \mathbf{A}\mathbf{d}) \quad (18)$$

and

$$\mathbf{D}' = (\mathbf{I} - \mathbf{D}\mathbf{A}^T\mathbf{G}\mathbf{A})\mathbf{D}(\mathbf{I} - \mathbf{A}^T\mathbf{G}\mathbf{A}\mathbf{D}) \\ + \mathbf{D}\mathbf{A}^T\mathbf{G}\mathbf{V}\mathbf{G}\mathbf{A}\mathbf{D}, \quad (19)$$

where

$$\mathbf{G} = \mathbf{V}_D^{-1} - \mathbf{V}_D^{-1}\mathbf{B}(\mathbf{B}^T\mathbf{V}_D^{-1}\mathbf{B})^{-1}\mathbf{B}^T\mathbf{V}_D^{-1} \quad (20)$$

$$\mathbf{V}_D = \mathbf{V} + \mathbf{A}\mathbf{D}\mathbf{A}^T, \quad (21)$$

and \mathbf{I} is the identity matrix of the same dimensions as \mathbf{D} . The matrix \mathbf{V}_D can be interpreted as sum of the covariance of the residuals due to measurement uncertainty and the covariance due to the alignment uncertainty. \mathbf{G} can be interpreted as a projection of the inverse of \mathbf{V}_D such that $\mathbf{G}\mathbf{B} = \mathbf{B}^T\mathbf{G} = 0$, in order to remove bias.

For some types of detector geometries, including that of the CVT, the residuals may depend non-linearly on the alignment parameters and/or the track parameters. Such non-linearity can lead to a systematic bias in the alignment parameters obtained by the KAA. We found that multiple iterations of the KAA, alternating with re-iterations of the event reconstruction with the updated alignment parameters, are necessary in order to converge on a non-biased set of alignment parameters. This differs from the use of KAA in CMS, where the exclusive use of parallel strips and planar sensors cause the residuals to depend linearly on the alignment parameters. For CMS, only a single pass of the KAA was necessary [5].

4. Datasets

We used two special calibration runs taken in spring, 2019 during an experiment with a 10.6 GeV electron beam on a 5 cm liquid-deuterium target. The first run was a “cosmic run”, which was taken by turning off the beam and the spectrometer’s magnetic field, and triggering on cosmic rays passing through the detector. The second run was in the “field-off” configuration: the electron beam was on with 5 nA, and the target was in place⁷, but the

⁷For this run, the target was in the “empty” configuration, *i.e.* depressurized so that almost all of the scattering took place on the

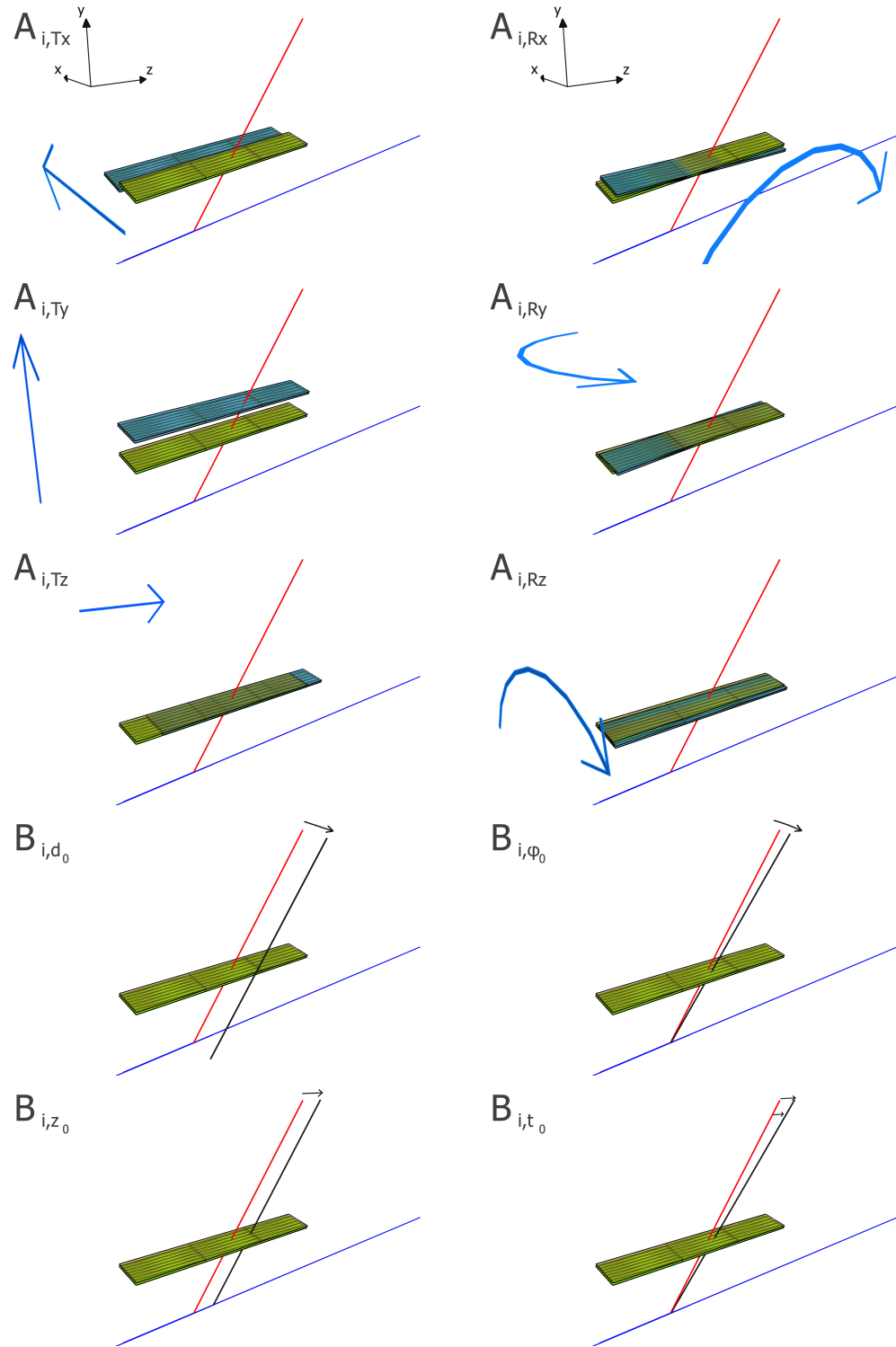
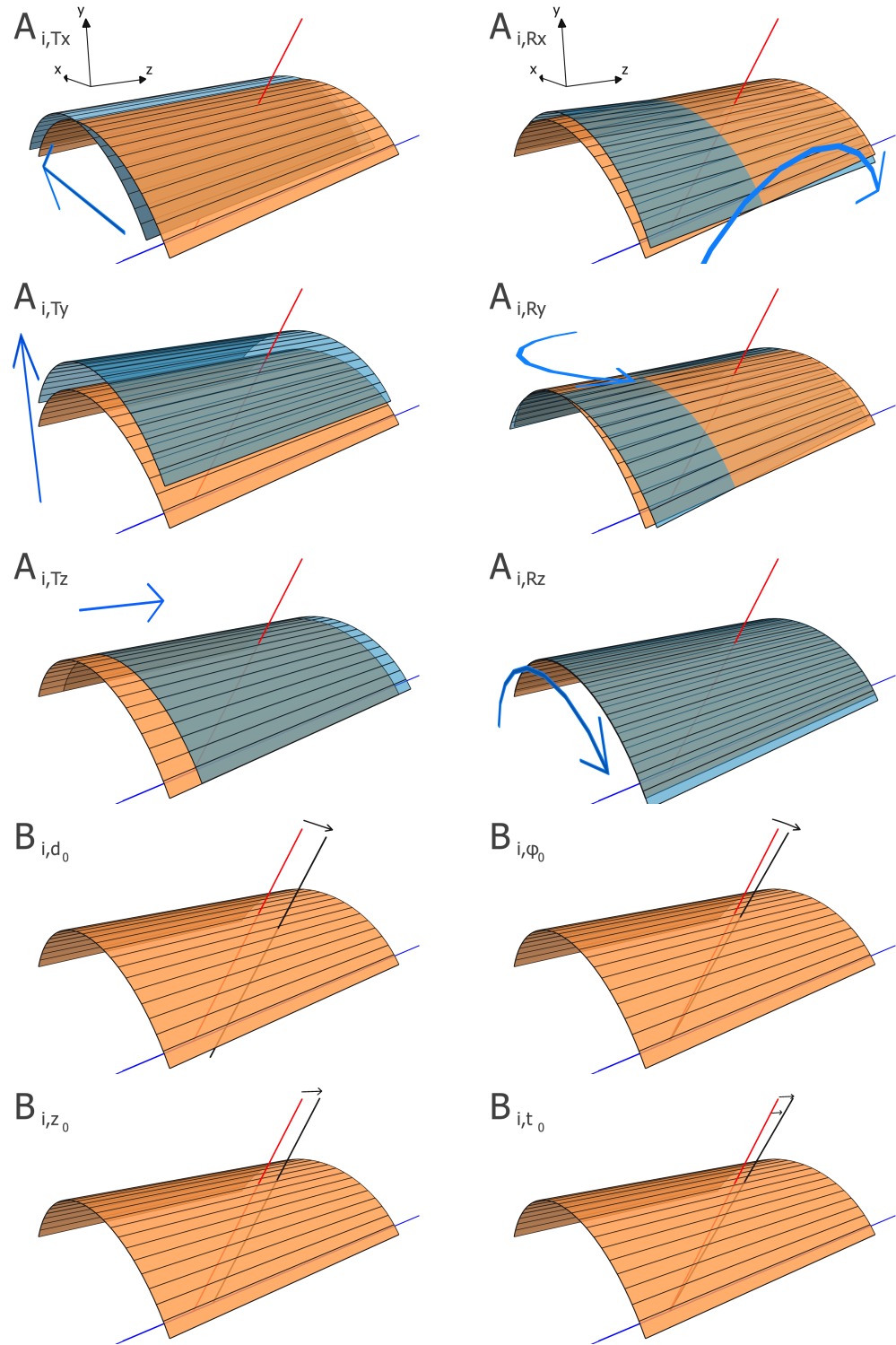


Figure 4: Illustration of matrix elements corresponding to translation degrees of freedom (top three panels, left column), rotation degrees of freedom (right column, top three panels), and variation in track parameters (bottom 2 rows) for one SVT module. The reference trajectory is shown in red, and the beamline is shown in blue. For the elements of the track-derivative matrix, \mathbf{B} , we show in black the trajectories with the indicated track parameter varied from the reference values.



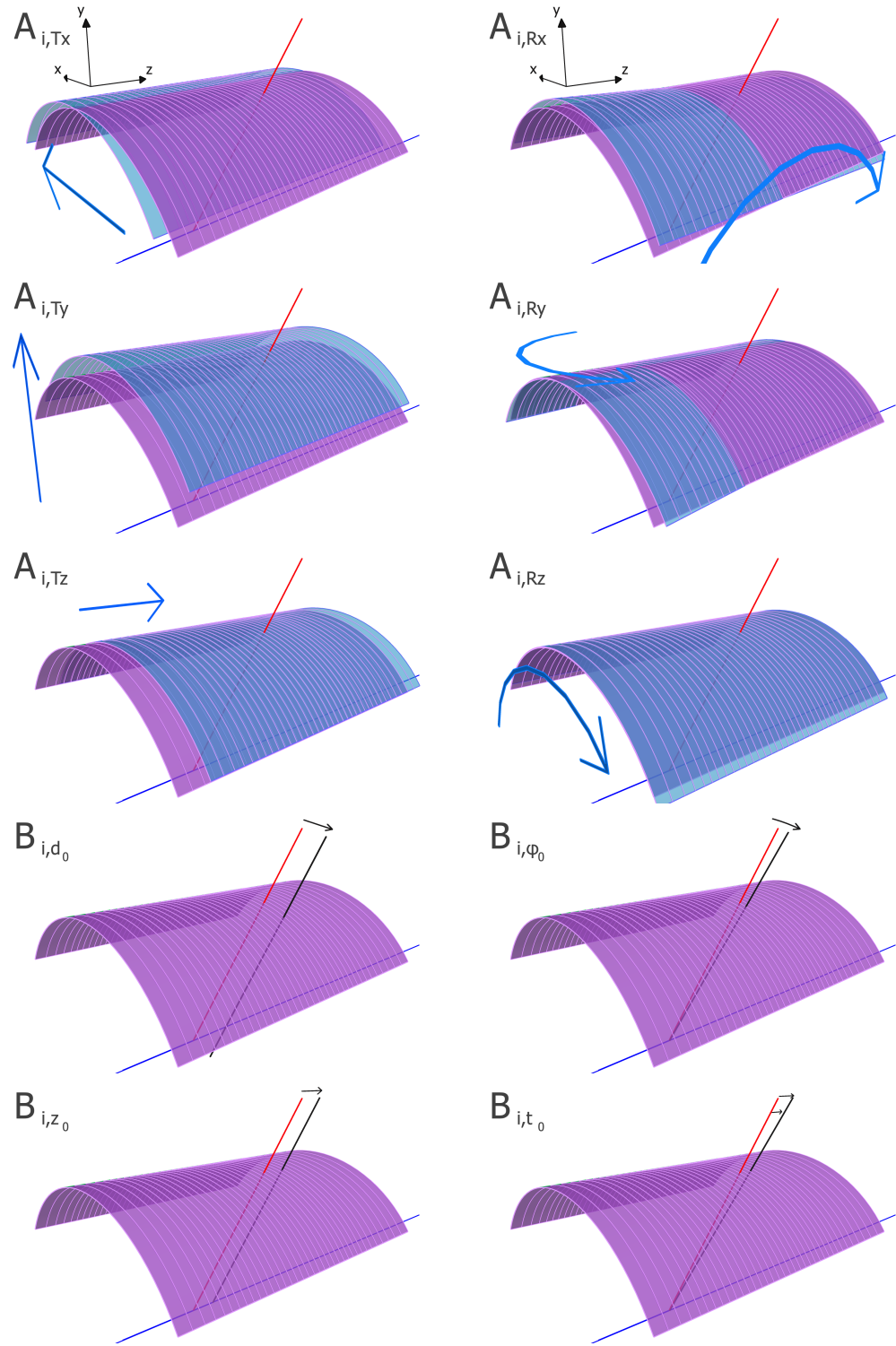


Figure 6: Illustration of matrix elements corresponding to translation degrees of freedom (top three panels, left column), rotation degrees of freedom (right column, top three panels), and variation in track parameters (bottom 2 rows) for one BMTc module. The reference trajectory is shown in red, and the beamline is shown in blue. For the elements of the track-derivative matrix, \mathbf{B} , we show in black the trajectories with the indicated track parameter varied from the reference values.

353 magnetic field was turned off. Example tracks from both 357
354 runs are shown in Fig. 7. 398

355 For both configurations, the particles' trajectories are 399
356 (neglecting multiple scattering) straight lines, which have 400
357 several advantages over using helical tracks. First, the 401
358 straight tracks can be described with fewer parameters 402
359 four parameters rather than the five parameters for a heli- 403
360 cal track. Second, no corrections need to be applied 404
361 due to a possible non-homogeneity of the magnetic field 405
362 Third, when the magnetic field is switched off, the Lorentz 406
363 effect in the BMT is non-existent [8], so no corrections 407
364 are needed for this effect. Finally, the formulas for the 408
365 derivative matrices \mathbf{A} and \mathbf{B} (see Eqs. 10-17) are simple 409
366 for straight tracks than for helices. 410

367 The two data-taking configurations each have their 411
368 strengths and weaknesses when used in alignment, so com- 412
369 bining both in our sample takes advantage of both of their 413
370 strengths. Since the cosmic tracks pass through both the 414
371 top half of the detector and the bottom half of the detec- 415
372 tor, they are useful for aligning the two halves together. 416
373 However, the cosmic tracks are less likely to pass through 417
374 the SVT modules on the sides of the detector mounted 418
375 vertically (ϕ near 0° or 180°) and do not provide infor- 419
376 mation about the alignment of the detector relative to
377 the beamline. The “field-off” tracks from the target have
378 a nearly uniform distribution in ϕ , and therefore have
379 reasonable statistics in all of the SVT sectors. Since such
380 tracks originate from the target, they can be used later
381 on to constrain the alignment of the detector relative to
382 the target and the beamline.

383 The BMTc, in particular, cannot be aligned using
384 only the tracks that originate from the beamline. This
385 is because each sector of the BMTc has a global weak
386 mode⁸ in which the three BMTc layers within the sector
387 are shifted along the beam direction by an amount
388 proportional to their radii. However, these weak modes
389 can be constrained by using the cosmic tracks, which do
390 not pass through the beamline. By including both types
391 of events in our sample, we remove the problematic weak
392 modes and have sufficient statistics in all of the modules
393 of the CVT.

394 Since the alignment procedure required rerunning the
395 CLAS12 event reconstruction on each data set multiple
396 times, we developed a procedure to create a sub-sample

containing only the events with tracks that would be used
in the KAA. First, we ran a preliminary event reconstruction
using the CLAS12 reconstruction package [12] with
a pre-aligned version of the detector geometry, which was
found using a detector survey followed by manual ad-hoc
adjustments to individual alignment parameters. We then
filtered out events that did not have tracks in the CVT.
Events with more than two tracks were also removed, in
order to get a cleaner sample. If the angle between the re-
constructed track direction and the normal of any sensor
used in reconstructing the track was more than 75° , or
if the magnitude of the vector \vec{s}' (see Eq. 8) was greater
than 10, then the whole track was rejected. These cuts re-
moved tracks that were difficult to accurately reconstruct
with the detector.

To further improve the quality of our selected tracks,
we required that all tracks had at least three BMTc clus-
ters, two BMTz clusters, and two pairs of clusters on
paired sensors in the SVT. Further, we rejected tracks
with very large residuals; these cuts were 7 mm for the
BMTz (which had the worst misalignments of the three
subsystems before the alignment), and 2 mm for the BMTc
and SVT.

target windows, and only a small part of the data sample was from
scattering from the residual gas. This way, the longitudinal position
of the target could be determined.

⁸that is, a degree of freedom that is either entirely unconstrained
or very poorly constrained.

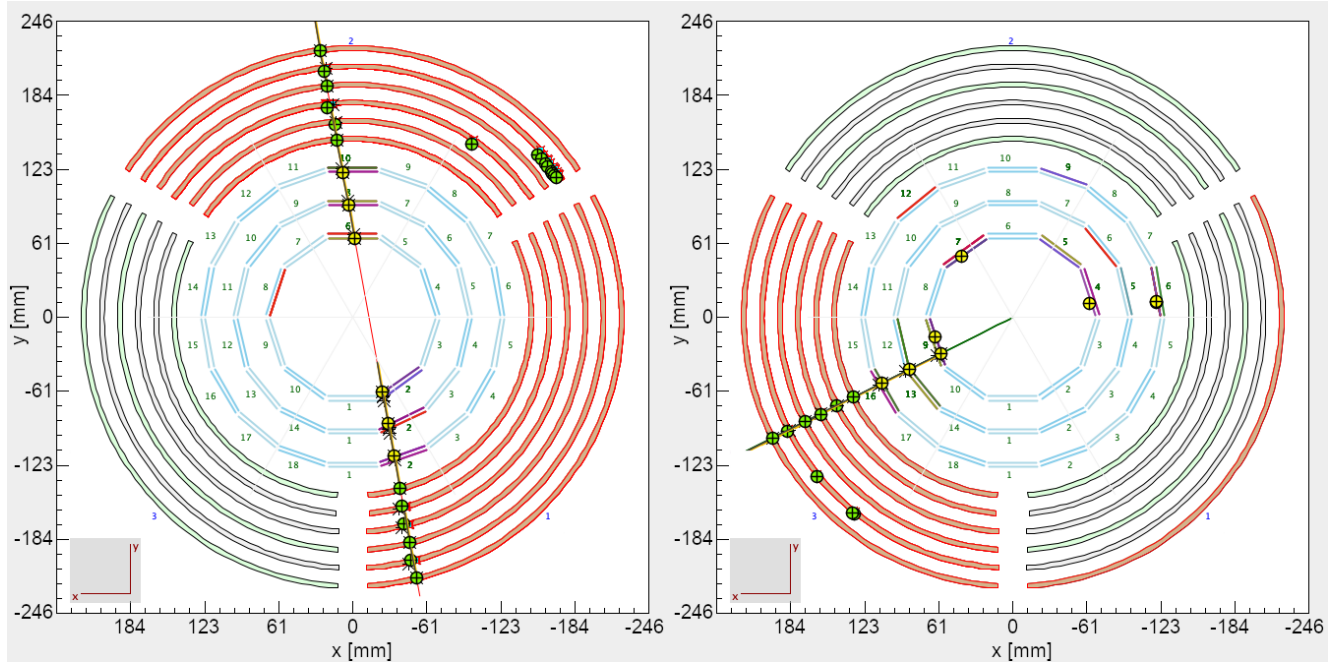


Figure 7: Example tracks from the “cosmic” (left) and “field-off” (right) configurations, as shown in the CLAS12 Event Display. Units are mm. BMT tiles that have been hit are outlined in red. A yellow circle with a + represents a reconstructed crossing between pairs of clusters on the two sensors in the same SVT module. The green circles represent the reconstructed position of BMT clusters (for BMTc, the azimuthal position is shown at the crossing of the track and the layer). An asterisk is shown behind the circles at the position where the fitted track intersects the sensors. The colors of the SVT sensors represent the ADC values of the hits on those sensors.

5. Aligning the CLAS12 CVT

The alignment procedure was comprised of several iterations of the following steps:

- Running the CVT part of the CLAS12 reconstruction package [12] using the alignment parameters from the calibration-constants database (CCDB).
- Running the KAA. This is not part of the CLAS12 reconstruction, but rather a stand-alone software package, which takes as input from the reconstruction step a set of track measurements along with the alignment and track-derivative matrices (Eqs. 10 and 11).
- Adjusting the values in the CCDB based on the output of the KAA.

For the track fitting part of the reconstruction, we ignored the effects of multiple scattering, which were used in the standard variation of reconstruction. We did this in order to avoid having an uneven weighting of hits in the outer layers during the fit, which would produce artificially large (small) residuals in the outer (inner) layers.

Several cycles were necessary because the KAA operates using a linear expansion of the track residuals’ dependence on the alignment parameters, as determined using the values of the alignment parameters at the time that the events were reconstructed, while the dependence in reality is non-linear, since the CLAS12 CVT contains non-parallel strips and curved sensors. Therefore, the alignment values obtained from a single iteration may have some bias, which can be ameliorated by multiple iterations.

We used an event sample that combines the cosmic and “field-off” event samples. In order to avoid any bias from having all of the events of one of these two types at the beginning of the event sample and all of the other type at the end of the sample, we randomized the order of the events before starting the KAA.

All three subsystems were fit simultaneously, rather than fitting them individually, since this takes into account the correlations between the the alignments of the different subsystems. At the beginning of each iteration, the diagonal elements of the covariance matrix \mathbf{D}_{init} were initialized to the following values:

462 • $\epsilon^2 = 10^{-14}$ for the elements corresponding to fixed
 463 parameters. This value is arbitrarily small, but non-
 464 zero in order to prevent \mathbf{D}_{init} from being singular.
 465 This includes translations in z for all BMTZ sensors
 466 and rotations in z for all BMTZ sensors. We also
 467 chose to fix all parameters for one of the BMTZ
 468 modules (layer 5, sector 2), so that all alignment
 469 parameters would be relative to this sensor. Since
 470 global translations in z would otherwise be a weak
 471 mode, we also fixed the translations in z for one of
 472 the BMTZ modules (layer 6, sector 2).
 473 • For the non-fixed parameters, we used the follow-
 474 ing values: $\Delta T^2 = (1.5 \text{ mm})^2$ for translations and
 475 $\Delta R^2 = (0.005 \text{ rad})^2$ for rotations. The values of
 476 ΔT and ΔR were chosen to be bit larger than the
 477 maximum uncertainty of the precision of the prelimi-
 478 nary survey⁹. It should be noted that due to the
 479 convergence of Kalman filter algorithms in general,
 480 overestimating the initial uncertainties has a very
 481 limited impact on the final results.

482 Since the SVT sensors are rigidly attached back-to-
 483 back with one another (see Fig. 2), the relative misalign-
 484 ment between paired sensors is much smaller than the
 485 alignment between different pairs or between the SVT
 486 modules and the BMT modules. We assumed that the
 487 alignments of the two sensors in a given SVT module only
 488 differ by translation transverse and longitudinal to the
 489 module (and had the same rotational alignment, as we
 490 as the same translation alignment normal to the sensors).
 491 Therefore, we introduced parameters $\Delta T_\ell = 0.01 \text{ mm}$ and
 492 $\Delta T_t = 0.01 \text{ mm}$ as the uncertainty in the relative longitu-
 493 dinal and transverse alignment within the pair. We then
 494 set the following off-diagonal elements:

- 495 • $\Delta R^2 - \epsilon^2/4$ for off-diagonal elements corresponding
 496 to the rotation about a given axis for one SVT sen-
 497 sor, and the rotation about the same axis for the
 498 other sensor in the same SVT module.
- 499 • $\Delta T^2 - (\epsilon^2 \cos^2 \phi + \Delta T_t^2 \sin^2 \phi)/4$, for the translations
 500 in x of one sensor and the translation in x of the
 501 other sensor in the pair. Here, ϕ is the nominal

⁹The survey had an estimated precision of a few hundred μm
 the global x and y directions) to 1 mm (in global z) for the
 internal alignment, and about 100-150 μm for internal alignment
 of the SVT (due to the use of fiducials for every module), and
 200 μm for the global SVT-BMT relative alignment. Here, we
 define internal alignment of a detector subsystem as the relative
 alignment between modules in that subsystem.

azimuthal coordinate of the midplane of the SVT sector.

- $\Delta T^2 - (\epsilon^2 \sin^2 \phi + \Delta T_t^2 \cos^2 \phi)/4$, for the translations
 in x of one sensor and the translation in x of the
 other sensor in the back-to-back pair.
- $(\epsilon^2 - \Delta T_t^2)/4 \sin \phi \cos \phi$, for the translations in y
 of one sensor and the translation in x of the other
 sensor in the back-to-back pair.
- $-(\epsilon^2 - \Delta T_t^2)/4 \sin \phi \cos \phi$, for the translations in y
 of one sensor and the translation in x of the same
 sensor.
- $\Delta T^2 - \Delta T_\ell^2/4$ for the translation in z in one sensor
 and the translation in z of the other sensor in the
 back-to-back pair.

Further, the inclusion of these constraints modifies the diagonal elements as well. Instead of ΔR^2 and ΔT^2 , the diagonal elements for the SVT are

- $\Delta R^2 + \epsilon^2/4$ for rotation parameters.
- $\Delta T^2 + (\epsilon^2 \cos^2 \phi + \Delta T_t^2 \sin^2 \phi)/4$ for translation pa-
 rameters in x .
- $\Delta T^2 + (\epsilon^2 \sin^2 \phi + \Delta T_t^2 \cos^2 \phi)/4$ for translation pa-
 rameters in y .
- $\Delta T^2 + T_\ell^2/4$ for translation parameters in z .

All other elements of \mathbf{D}_{init} , besides those listed above, were set to zero.

Since there are 6 parameters per module and 84 SVT sensors and 18 BMT sensors, there are $6 \times (84 + 18) = 612$ total parameters. However, considering the fact that six parameters are fixed for global alignment, and four are fixed per SVT sensor pair, and one parameter is fixed for each BMT sensor, the remaining number of degrees of freedom is 420.

6. Results

To align the detector using the cosmic-ray and “field-off” data from the Spring 2019 run, we followed the procedure detailed in Sec. 5 for running the KAA with multiple iterations. The KAA provides the alignment parameters needed to correct for errors in the reconstructed particle tracks, thus minimizing the residuals of the track reconstruction when those corrections are applied.

The distributions of residuals¹⁰ of the sampled tracks before (red, dashed) and after (black, solid) alignment are shown in Fig. 8 for the SVT (a), BMTZ (b), and BMTZ (c). In each detector, the residual distributions after alignment are much narrower than those before the alignment. We then determined the full widths at half maximum (FWHMs) of these distributions, which are 116 μm for the SVT, 432 μm for the BMTZ, and 248 μm for the BMTZ. Similarly, we also fit the cores of the distributions to Gaussian functions and obtained values that are about half of the values of the FWHMs¹¹: 57, 230 and 180 μm for the SVT, BMTZ, and BMTZ, respectively. These are comparable to the expected spatial resolutions of the SVT and BMT from Refs. [7] and [8], respectively. The means of these distributions are on the order of a few μm , which is acceptable. The measured resolutions are consistent with the system design goal of momentum resolution below 5% for charged particles with momenta up to 1 GeV in stand-alone SVT reconstruction [7].

We calculated the χ^2 for each track as

$$\chi^2 = \mathbf{r}^T \mathbf{V}^{-1} \mathbf{r}, \quad (22)$$

where the number of degrees of freedom, n_{dof} , is the number of clusters in the track minus four (since there are four parameters for the track fit). The distributions of the χ^2/n_{dof} values before and after alignment are shown in Fig. 8(d). As shown in Fig. 9, the average χ^2/n_{dof} goes down from 10.0 to about 3.4 after the first iteration, and down to about 2.8 after the second. There is a very small improvement (<0.1) after the third iteration. After the fourth and fifth iterations, there is no significant change to the average χ^2/n_{dof} . Based on this assessment, there is no need to run the KAA for more than three iterations.

Since the residual distributions in Fig. 8 are the sum over the residual distributions in all of the sensors of each given type, it does not provide information about the alignment of individual sensors. Therefore, we determined the residual distributions of every sensor module individually in order to make sure that none of them had large misalignments. We then determined the means and FWHMs of these distributions, which we show in Fig. 10. After fitting, the means of the residual distributions for all sensors are within 20 μm of zero, and the FWHM are less than 170 (460) μm for each of the SVT (BMTZ) sensors.

¹⁰As defined by Eq. 7.

¹¹The ratio of the FWHM to the standard deviation of a distribution depends on its shape. For reference, this ratio is ≈ 2.35 for a Gaussian distribution.

The alignment process can become biased to show lower performance for certain track locations due to data sampling and the specific algorithm implementation. In order to show that there is no bias in the alignment, we studied the dependence of the residuals on the track parameters. Figure 11 shows the residuals for each of the three detector types as a function of the track kinematic variables d_0 , ϕ_0 , z_0 and t_0 . The residual distributions after the alignment procedure are centered at zero, with no significant dependence on the kinematic variables.

The KAA algorithm also yields the correlation among the alignment parameters. The correlations are given by the matrix \mathbf{C} , where each element is given by

$$C_{ij} = D_{ij} / \sqrt{D_{ii} D_{jj}}, \quad (23)$$

where \mathbf{D} is the covariance matrix. By construction, the diagonal elements of \mathbf{C} are equal to one. Many of the parameters are strongly correlated with one another, leading to off-diagonal elements of \mathbf{C} close to +1 (-1) when the correlations are strongly positive (negative). We show plots of the values of the elements of \mathbf{C} in Appendix A and discuss there in further detail which types of parameters are strongly or weakly correlated.

In order to see if the residual distributions depend on where the particles cross the sensors, we plot in Appendix B.1 the distributions of the residuals versus the extrapolated lab-frame coordinates of the hits in the detectors, both before and after the alignment. We also include the residuals versus the measured centroid strip number of the hits in each cluster. We found that the residual distributions after alignment appear to be centered at zero regardless of the position of the hit in the detector.

With an unaligned detector, the residuals in one sensor may be strongly correlated to those in another, whereas with a well-aligned detector, such correlations vanish. In Appendix B.2, we plot distributions of the residuals in one sensor versus those of another, for several different representative combinations of sensors. The 2D residual distributions show strong correlation for some of these combinations before alignment, but there is no significant correlation between the residuals after alignment.

To validate our results, we performed the same procedure on Monte-Carlo (MC) simulations, and present the results in Appendix C. In the simulations, the means of the residual distributions are within about 15 μm of zero, which is comparable to the data. However, the residual distributions are considerably narrower in the simulations than in the data, and as a result the χ^2/n_{dof} distribution in the simulation has a smaller mean than in the data.

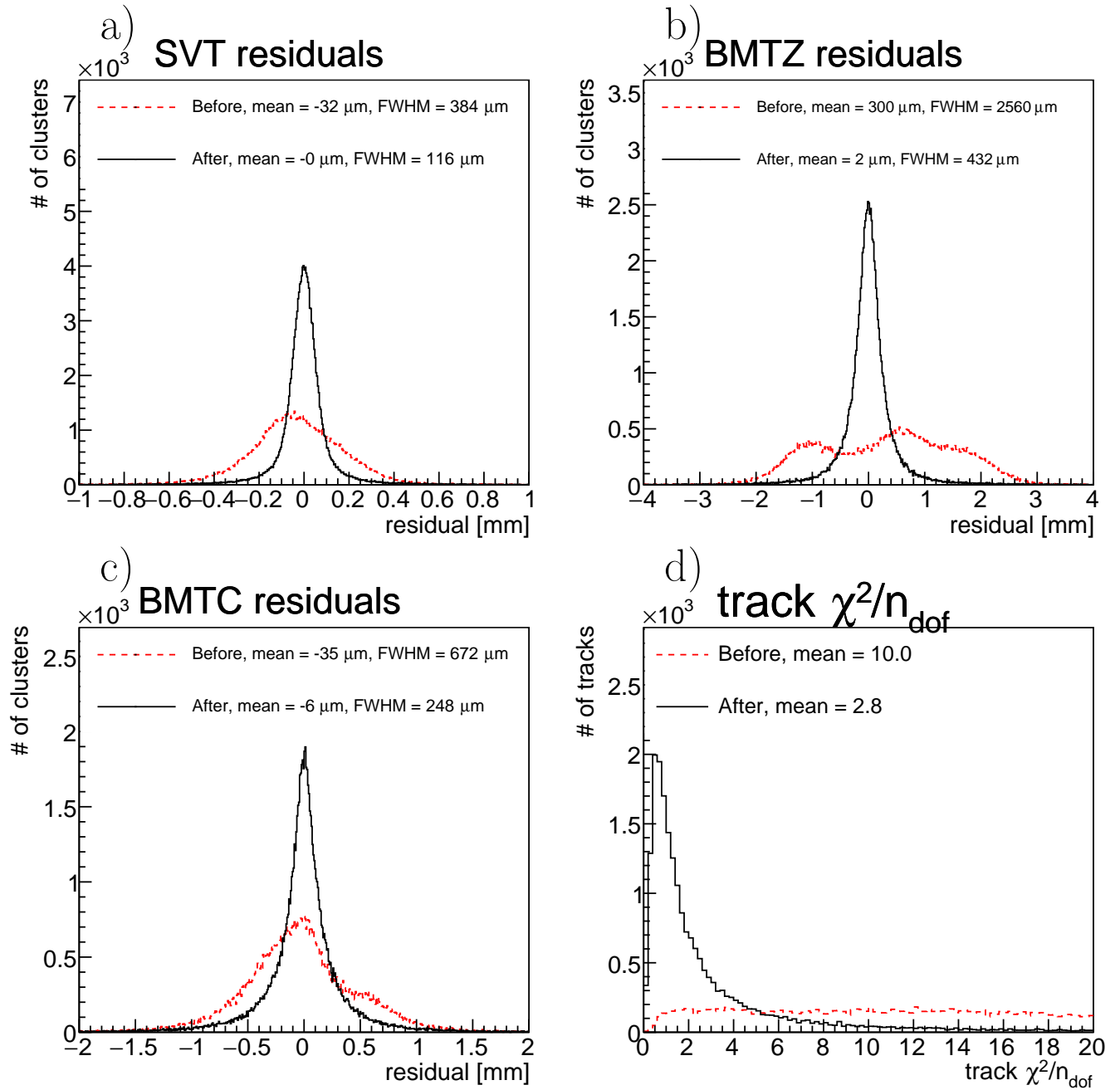


Figure 8: Residuals distribution before (red, dashed) and after (black, solid) alignment for the SVT (a), BMTZ (b) and BMTC (c). Panel (d) shows the χ^2/n_{dof} distribution (bottom right) for each reconstructed track. Each cluster produces a single residual for a single track.

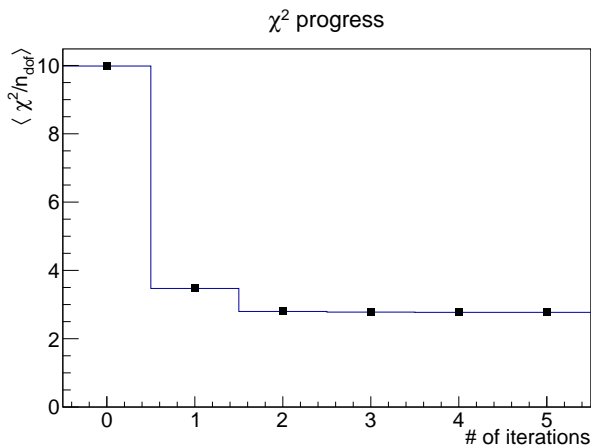


Figure 9: Average track χ^2/n_{dof} after the indicated number of iterations of the KAA. The first point (at zero iterations) represents the average track χ^2/n_{dof} before running any alignment with the KAA.

This could be due to a mis-modeling of the resolution effects in the detector, since the resolutions in the simulation were estimated using an idealized detector.

Finally, we validated that the alignment works not only for straight tracks, but also for curved tracks (with the solenoid field turned on), using the following test. Using a run configuration with 5 nA on liquid hydrogen at 10.2 GeV, we reconstructed events where electrons scattered elastically off a proton. These were selected by requiring one electron in the Forward Detector of CLAS12, with $W < 1.1$ GeV¹², *i.e.* in the elastic-peak region, and at least one positive track in CVT, which was assumed to be a proton. We show the distribution of the reconstructed polar angle θ vs the reconstructed momentum p of the protons in these reactions in Fig. 12, before (left) and after (right) the alignment procedure. The expected relation between θ_p and p_p for protons in elastic kinematics is:

$$p_p = \frac{2E_b m_p (E_b + m_p) \cos \theta_p}{E_b^2 \sin^2 \theta_p + 2E_b m_p + m_p^2}, \quad (24)$$

where m_p is the mass of a proton, and $E_b=10.2$ GeV is the beam energy; we show this as a curve overlaid on the distribution in Fig. 12. The θ vs. p distribution obtained after the alignment follows the curve much more closely than the one obtained before the alignment.

¹² W is defined as $\sqrt{2m_p \nu + m_p^2 - Q^2}$, where Q^2 is the square of the four-momentum transfer of the reaction, ν is the energy transfer and m_p is the proton mass.

7. Conclusions

We have adapted the KAA, originally developed for CMS, to align the CLAS12 CVT—a hybrid detector consisting of both silicon and micromegas tracking technologies, with both curved and non-parallel strips.

Using a sample of cosmic-ray tracks and “field-off” data, we obtained residual distributions centered within 10 μm of zero for each of the silicon and micromegas sensors. In order to avoid significant bias from the non-linearity of the detector geometry, we had to run multiple iterations of the alignment, re-running the event reconstruction with the updated alignment parameters in between iterations.

By adapting the algorithm to the CLAS12 CVT, we demonstrated the flexibility and power of the KAA [3, 4]. Future work will include extending these results to include the CLAS12 forward detectors or curved tracks as additional constraints.

The methodology and results detailed in this work could serve as reference for alignment of the CLAS12 CVT for upcoming experiments [13, 14], as well as for future experiments at the Electron-Ion Collider [15].

Acknowledgements

We acknowledge the outstanding efforts of the staff of the Accelerator, the Nuclear Physics Division, Hall B, and the Detector Support Group at JLab that have contributed to the design, construction, installation, and operation of the CLAS12 detector. We thank Maurizio Ungaro for his contributions in the CLAS12 simulations. We also thank the CLAS Collaboration for staffing shifts and taking high quality data. This work was supported by the United States Department of Energy under JSA/DOE Contract DE-AC05-06OR23177. This work was also supported in part by the U.S. National Science Foundation, the State Committee of Science of the Republic of Armenia, the Chilean Agencia Nacional de Investigación y Desarrollo, the Italian Istituto Nazionale di Fisica Nucleare, the French Centre National de la Recherche Scientifique, the French Commissariat à l’Energie Atomique, the Scottish Universities Physics Alliance (SUPA), the United Kingdom Science and Technology Facilities Council (STFC), the National Research Foundation of Korea, the Deutsche Forschungsgemeinschaft (DFG), and the Russian Science Foundation. This research was funded in part by the French Agence Nationale de la Recherche contract no. 37. This work was supported as well by the EU Horizon 2020 Research and Innovation Program

Residuals (all modules)

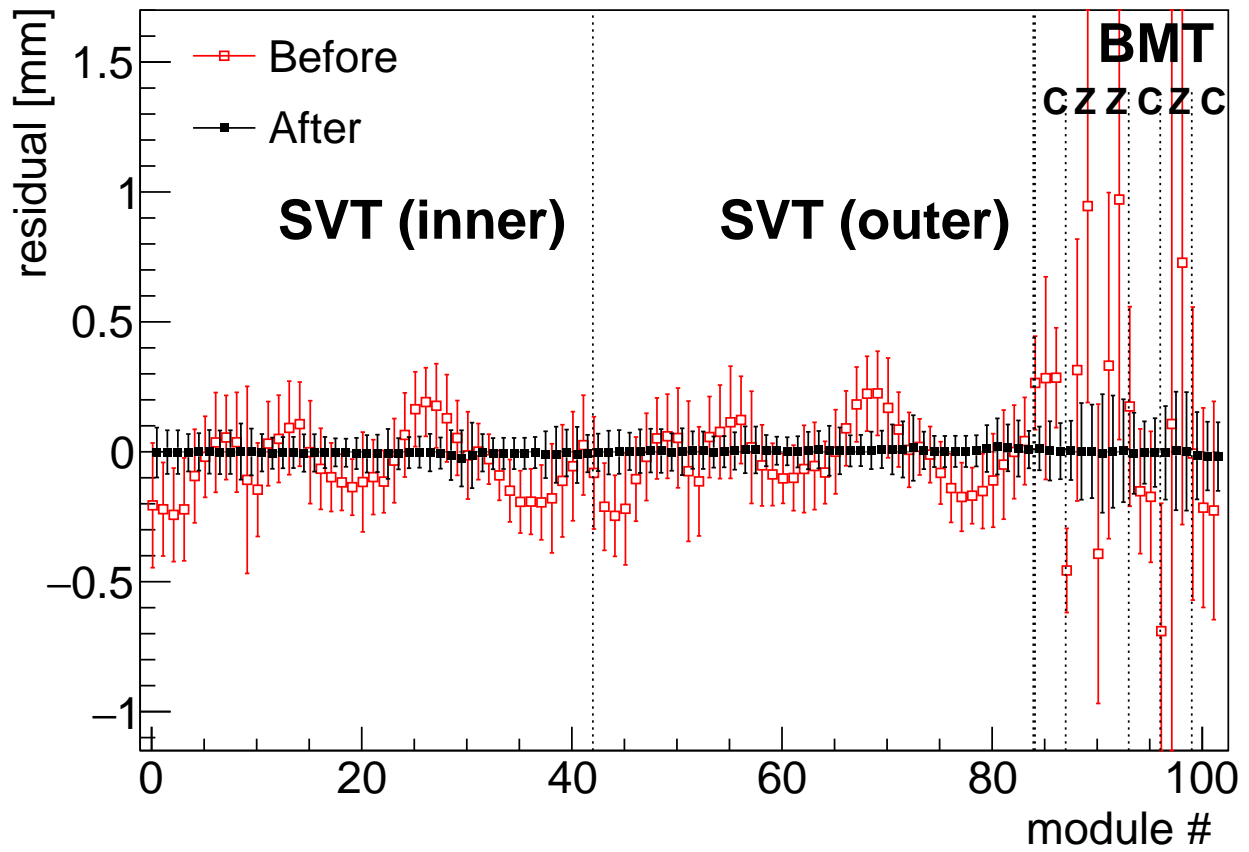


Figure 10: Residuals for the each module, before (red, open symbols) and after (black, closed symbols) alignment. The error bars for each point represent the FWHMs of the distributions, divided by two (so that the distance from the top of the upper error bar to the bottom of the lower error bar is one FWHM). Module numbers 1-84 represent SVT sensors; numbers 85-102 represent BMT tiles. Symbols are shifted horizontally slightly for clarity.

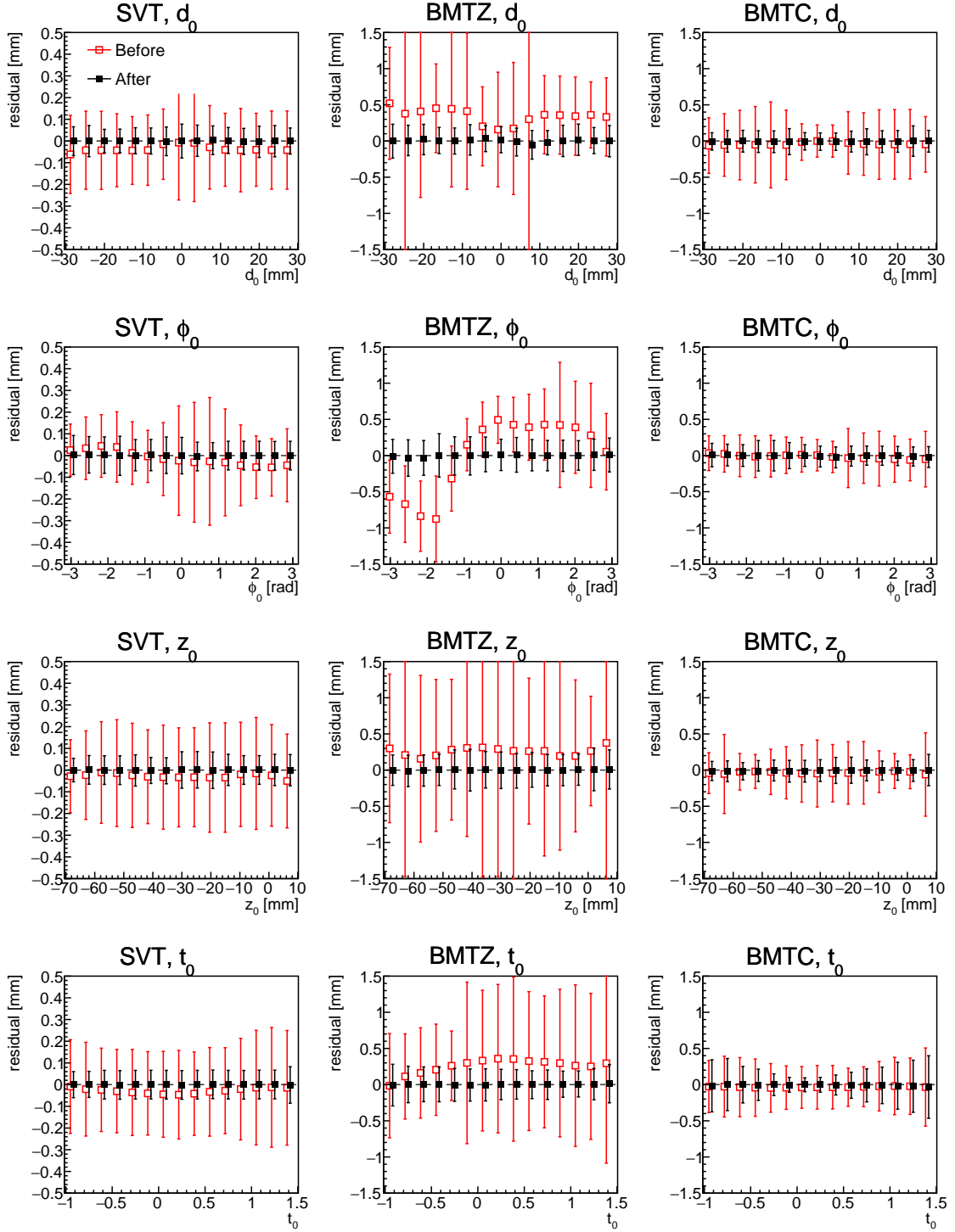


Figure 11: Residuals before (red, open symbols) and after (black, closed symbols) alignment, as a function of the kinematic variables: from top to bottom, d_0 , ϕ_0 , z_0 and t_0 . The error bars for each point represent the FWHMs of the distributions, divided by two (so that the distance from the top of the upper error bar to the bottom of the lower error bar is one FWHM). From left to right, the results are shown for the SVT, BMTZ, and BMTC. Symbols are shifted horizontally slightly for clarity.

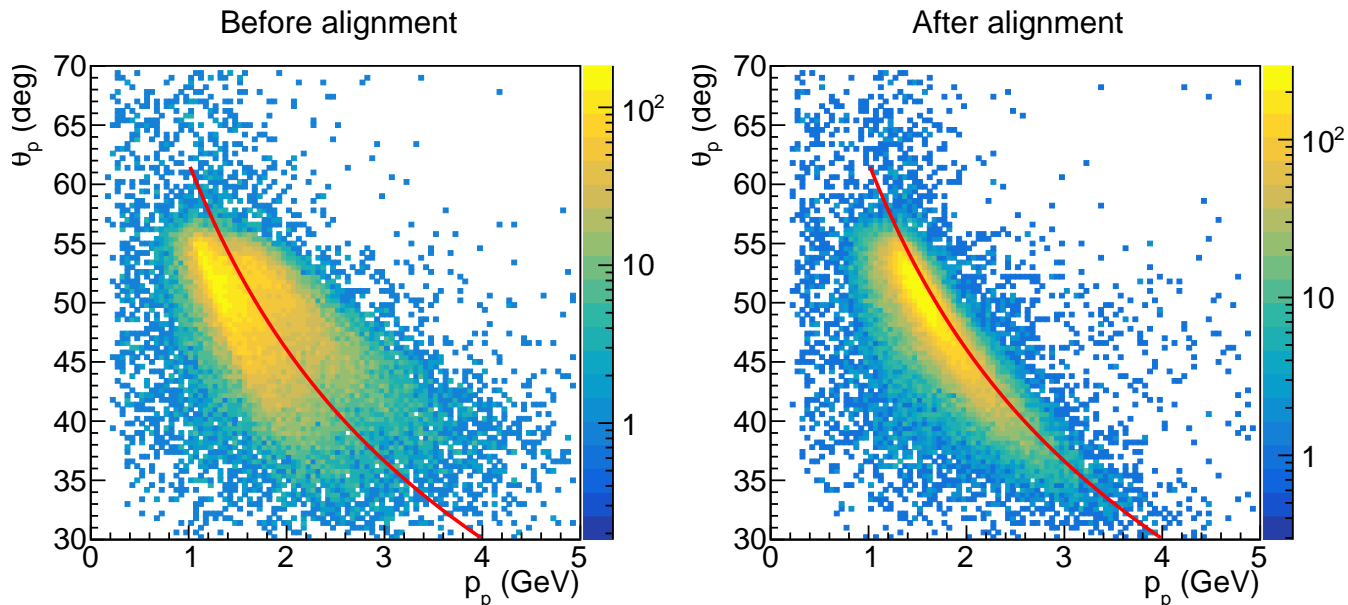


Figure 12: Polar angle vs. momentum distributions for elastically scattered protons in the CVT, before (left) and after (right) the alignment. The curve shows the expected correlation between the two variables.

684 under the Marie Skłodowska-Curie Grant Agreement No. 705
 685 101003460. 706

686 We also thank Martin Weber for developing a software
 687 implementation of the Kalman Alignment Algorithm and 707
 688 making it publicly available. 708

689 References 711

690 [1] V. Karimaki, T. Lampen, F. P. Schilling, The HIP 712
 691 algorithm for track based alignment and its applica- 713
 692 tion to the CMS pixel detector CERN-CMS-NOTE- 714
 693 2006-018 (Jan. 2006). 715

694 [2] V. Blobel, Software alignment for tracking detectors, 716
 695 Nucl. Instrum. Meth. A 566 (2006) 5–13. doi:10.1016/j.nima.2006.05.157. 717
 696 718

697 [3] E. Widl, R. Frühwirth, W. Adam, A Kalman filter 719
 698 for track-based alignment CERN-CMS-NOTE-2006- 720
 699 022 (1 2006). 721

700 [4] E. Widl, Global Alignment of the CMS Tracker, 723
 701 Ph.D. thesis, Vienna, Tech. U., CERN-THESIS- 724
 702 2008-123, CMS-TS-2008-026 (2008). 725

703 [5] E. Widl, R. Frühwirth, Application of the Kalman 726
 704 Alignment Algorithm to the CMS tracker, Journal of 727

of Physics: Conference Series 219 (3) (2010) 032065.
 doi:10.1088/1742-6596/219/3/032065.

[6] V. D. Burkert, *et al.* (CLAS12 Collaboration), The CLAS12 Spectrometer at Jefferson Laboratory, Nucl. Instrum. Meth. A 959 (2020) 163419. doi:10.1016/j.nima.2020.163419.

[7] M. Antonioli, *et al.*, The CLAS12 silicon vertex tracker, Nucl. Instrum. Meth. A 962 (2020) 163701. doi:https://doi.org/10.1016/j.nima.2020.163701.

[8] A. Acker, *et al.*, The CLAS12 micromegas vertex tracker, Nucl. Instrum. Meth. A 957 (2020) 163423. doi:https://doi.org/10.1016/j.nima.2020.163423.

[9] R. Antunes-Nobrega, *et al.* (LHCb Collaboration), LHCb reoptimized detector design and performance: Technical Design Report, Technical design report. LHCb, CERN, Geneva, 2003. URL https://cds.cern.ch/record/630827

[10] S. Viret, C. Parkes, M. Gersabeck, Alignment procedure of the LHCb vertex detector, Nucl. Instrum. Meth. A 596 (2) (2008) 157–163. doi:https://doi.org/10.1016/j.nima.2008.07.153.

- 728 [11] R. Frühwirth, Application of kalman filtering to track
729 and vertex fitting, Nucl. Instrum. Meth. A 262 (2)
730 (1987) 444–450. doi:[https://doi.org/10.1016/](https://doi.org/10.1016/0168-9002(87)90887-4)
731 [0168-9002\(87\)90887-4](https://doi.org/10.1016/0168-9002(87)90887-4). 775
- 732 [12] V. Ziegler, *et al.*, The CLAS12 software frame-
733 work and event reconstruction, Nucl. Instrum. Meth.
734 A 959 (2020) 163472. doi:[https://doi.org/10.](https://doi.org/10.1016/j.nima.2020.163472)
735 [1016/j.nima.2020.163472](https://doi.org/10.1016/j.nima.2020.163472). 776
- 736 [13] V. D. Burkert, Jefferson lab at 12 GeV: The sci-
737 ence program, Annual Review of Nuclear and Par-
738 ticle Science 68 (1) (2018) 405–428. doi:[10.1146/](https://doi.org/10.1146/annurev-nucl-101917-021129)
739 [annurev-nucl-101917-021129](https://doi.org/10.1146/annurev-nucl-101917-021129). 777
- 740 [14] J. Arrington, *et al.*, Physics with CEBAF at 12 GeV
741 and Future Opportunities ArXiv:2112.00060 (Nov.
742 2021). arXiv:[2112.00060](https://arxiv.org/abs/2112.00060). 778
- 743 [15] R. Abdul Khalek, *et al.*, Science Requirements and
744 Detector Concepts for the Electron-Ion Collider:
745 EIC Yellow Report BNL-220990-2021-FORE, JLAB
746 PHY-21-3198, LA-UR-21-20953 (3 2021). arXiv:
747 [2103.05419](https://arxiv.org/abs/2103.05419). 779
- 748 [16] M. Ungaro, *et al.*, The CLAS12 Geant4 simulation
749 Nucl. Instrum. Meth. A 959 (2020) 163422. doi:
750 [10.1016/j.nima.2020.163422](https://doi.org/10.1016/j.nima.2020.163422). 780
- 751 [17] S. Agostinelli, *et al.* (*GEANT4 Collaboration*),
752 GEANT4—a simulation toolkit, Nucl. Instrum.
753 Meth. A 506 (2003) 250–303. doi:[10.1016/](https://doi.org/10.1016/S0168-9002(03)01368-8)
754 [S0168-9002\(03\)01368-8](https://doi.org/10.1016/S0168-9002(03)01368-8). 781

755 Appendix A. Correlations

756 The values of the elements of the correlation matrix \mathbf{C}
757 (see Eq. 23), at the end of the final iteration, are shown
758 in Fig. A.13. We also show a zoom-in of the BMT part
759 of this matrix in Fig. A.14. 803

760 We find that the alignment parameters for any of the
761 BMTC sensors are always very strongly positively cor-
762 related with the same parameters for the other BMTC
763 sensors in the same sector. This is apparent in Fig. A.14
764 as visible as dark red diagonal streaks, such as the one
765 near the bottom right corner starting in row 594 (marked
766 with an ellipse in Fig. A.14), correlating BMTC layers 1
767 and 6. The BMTC parameters are very weakly correlated
768 with the parameters of the SVT and the BMTZ, which
769 are apparent in Figs. A.13 and A.14 as blocks of mostly
770 white, suggesting that the internal alignment within the
771 BMTC is much better than its alignment relative to the 804

other components. This is largely due to the fact that the
BMTC measures the position of the track in z , which is a
weak mode for the BMTZ. Translations in z are also less
strongly constrained by the SVT than the BMTZ, since
the BMTZ has much better precision on the z positions
of tracks than crosses between clusters in the SVT.

Also, there is a strong correlation between the rota-
tions in x and y for a given SVT sensor and the rotation
in z for the same sensor. This is because the rotations
are defined around the CLAS12 origin, rather than the
center of the sensors, and the widths of the sensors are
much smaller than the distance between them and the
beamline. It is therefore difficult to distinguish between
a rotation around the global z axis and a translation of
the sensor plane in the azimuthal direction. 805

802 Appendix B. Additional plots

803 Appendix B.1. Residuals versus coordinates

To see if the residuals depend on the location where
the particles cross the sensors, we include plots of the
tracking residuals versus the global ϕ and z coordinates
of these intersection points in Figs. B.15 and B.16, respec-
tively. We show residuals versus the measured centroid
strip numbers in the sensors in Fig. B.17. The results
before (after) alignment are shown in the top (bottom)
row. There is a huge dependence of the residuals on the
 ϕ coordinate in the hit (see Fig. B.15), but this vanishes
after the alignment. Since the centroid number correlates
with ϕ in the BMTZ and the SVT, one would expect to
see a similar dependence on the centroid number, but this
would only be visible when looking at each sector individ-
ually. 806

807 Appendix B.2. Correlations between residuals in different 808 sensors

To determine if the residuals in different sensors in the
CVT are correlated to one another, we show in Fig. B.18
and B.19 some 2D distributions of the residuals for vari-
ous combinations of sensors, before (middle column) and
after (right column) alignment. For reference, the po-
sitions of the two sensors are shown to the left of the
2D residual plots. The 2D residual distributions show
strong correlations for some of these combinations before
alignment, especially when the sensors’ measurement di-
rections, \hat{s} , are parallel or nearly parallel to one another,
for instance between stereo pairs of SVT sensors (see first
row of Fig. B.18). In cases where the sensors’ measure-
ment directions are perpendicular to one another, such 809

correlation matrix

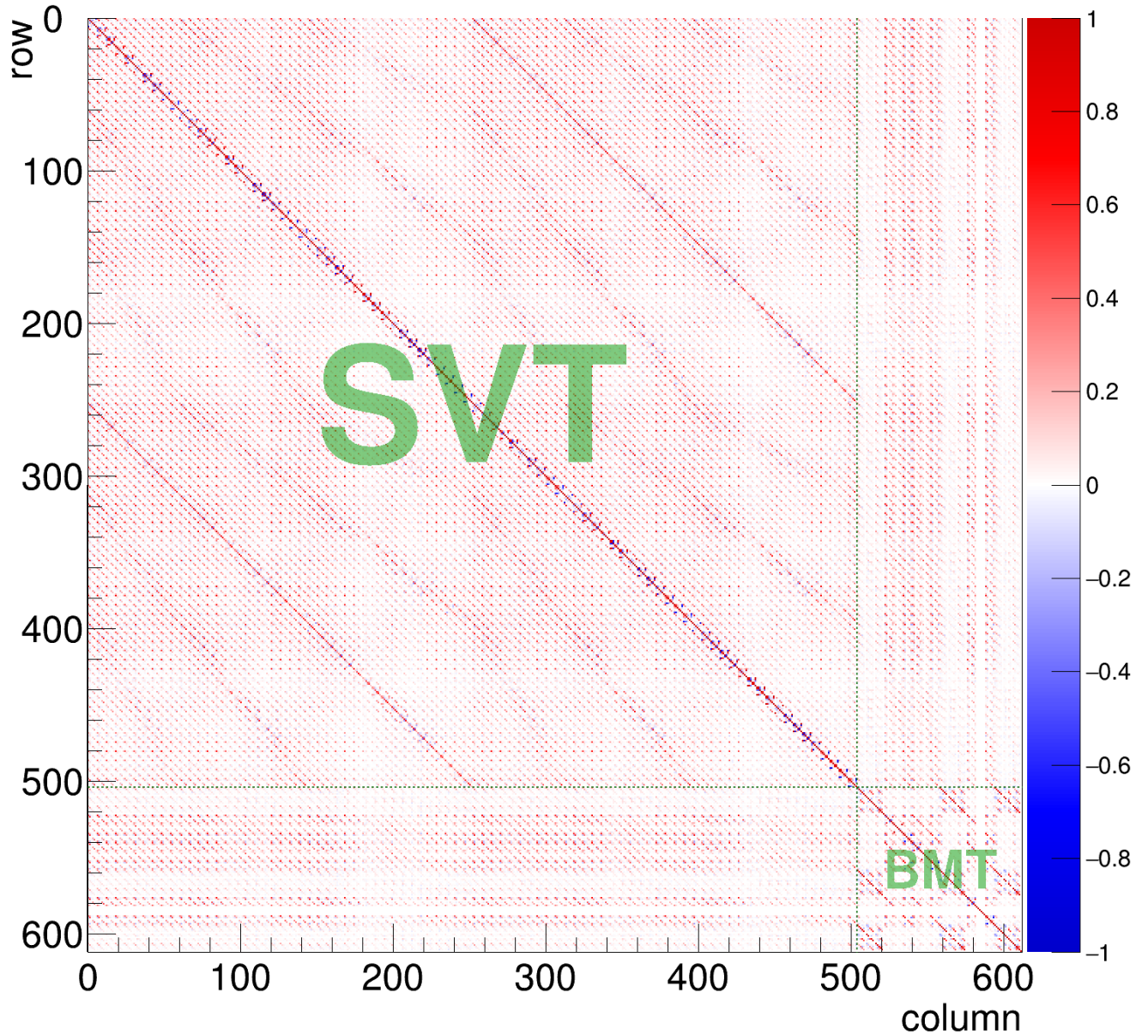


Figure A.13: Values of the matrix elements in the correlation matrix C . Every group of 6 indices represent translations in x , y and z and rotations in x , y and z of a single sensor. The first 84 of these groups represent the SVT, while the next 18 represent the BMT. Positive values are shown in red and negative values are shown in blue. The dark-green horizontal and vertical dotted lines demarcate the SVT and BMT regions.

correlations (bmt)

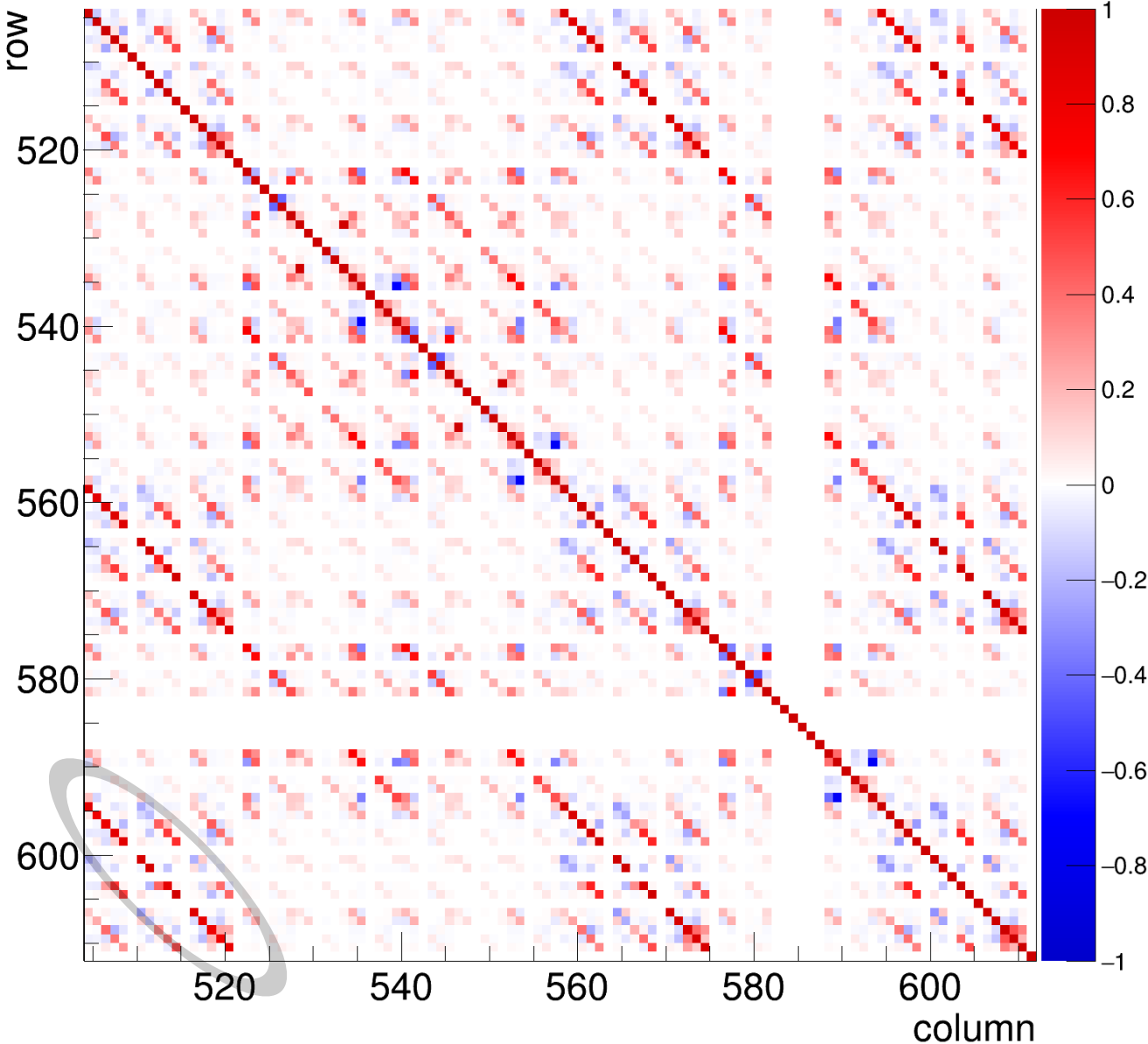
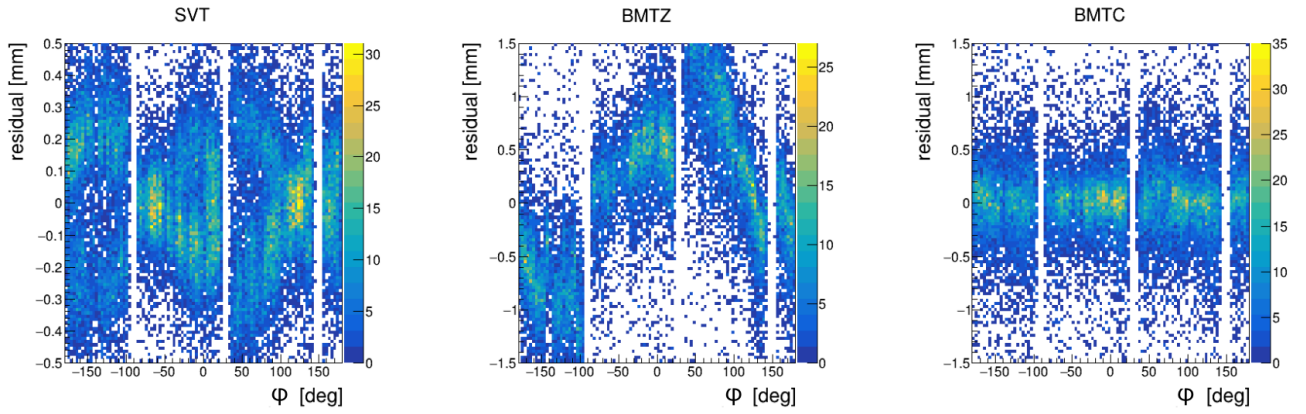


Figure A.14: Zoom-in of Fig. A.13, showing the submatrix of the correlation matrix \mathbf{C} corresponding to correlations between BMT alignment variables. Positive values are shown in red and negative values are shown in blue. The ellipse indicates one of the diagonal “streaks” mentioned in the text.

BEFORE



AFTER

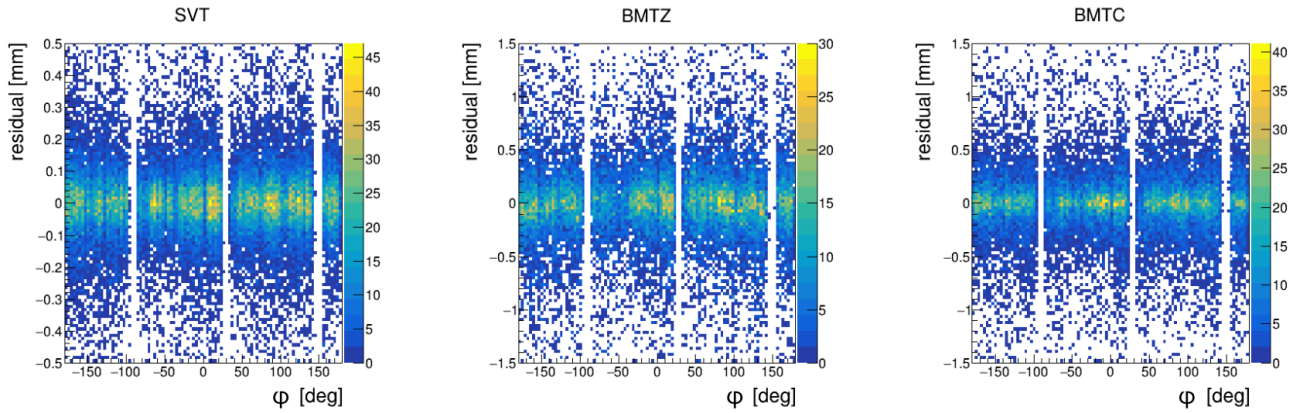


Figure B.15: Distributions of the residuals for SVT, BMTZ, and BMTC (left to right) vs. the ϕ coordinate of the extrapolated hit positions before (top row) and after (bottom row) the alignment.

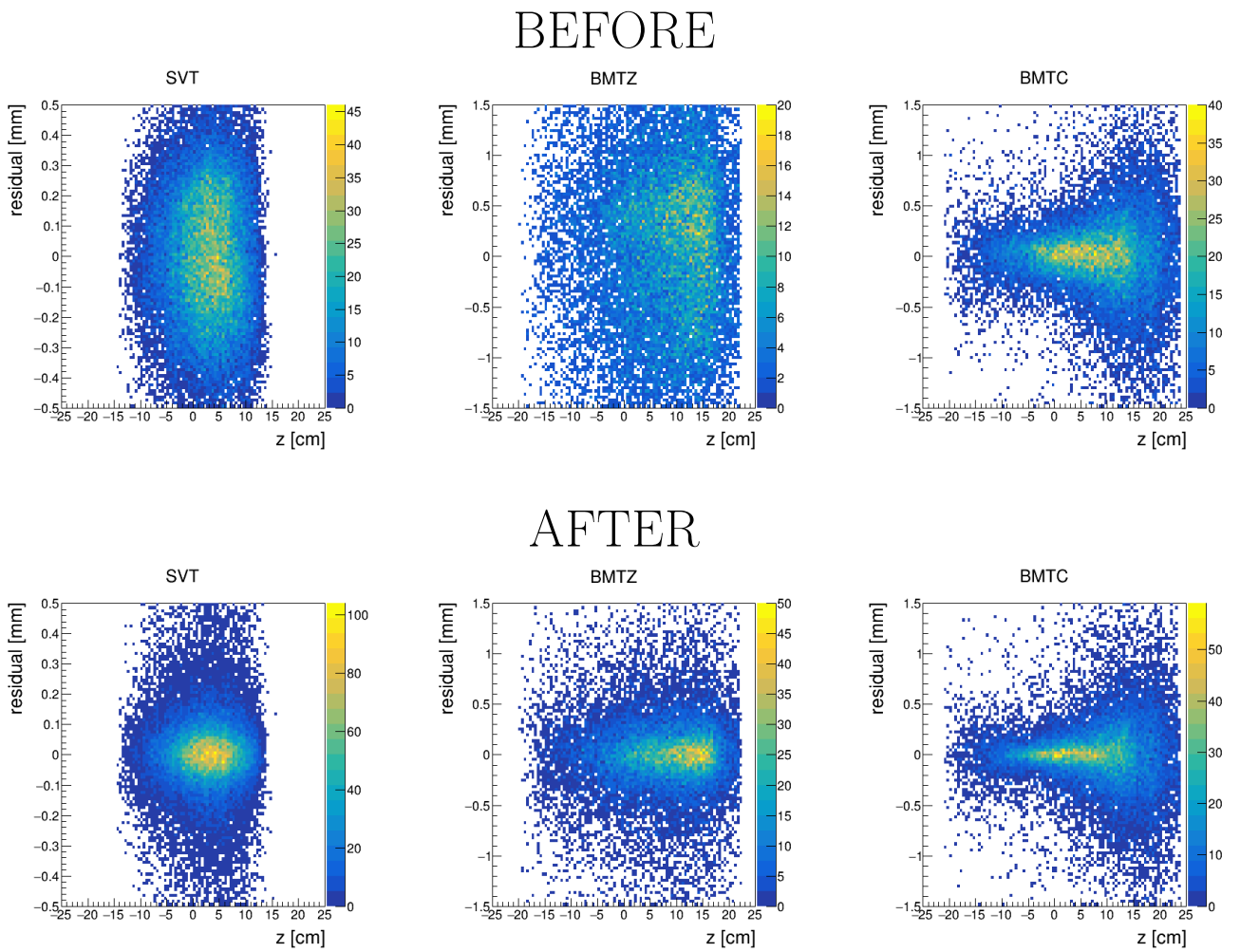


Figure B.16: Distributions of the residuals for SVT, BMTZ, and BMTC (left to right) vs. the z coordinate of the extrapolated hit positions before (top row) and after (bottom row) the alignment.

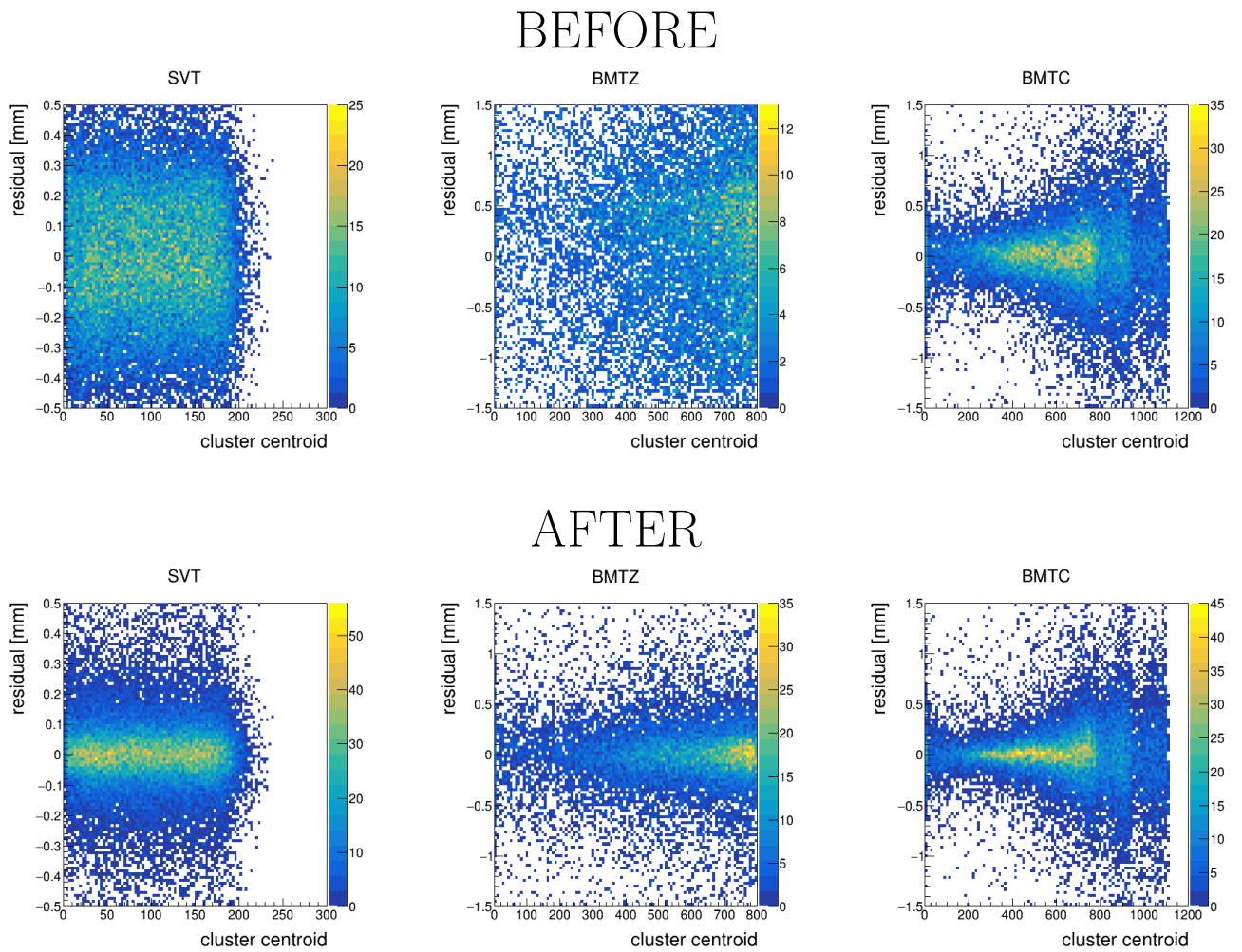


Figure B.17: Distributions of the residuals for SVT, BMTZ, and BMTC (left to right) vs. the centroid strip numbers of the measured events before (top row) and after (bottom row) the alignment.

818 as one sensor in the BMTC and another in the BMTZ 866
 819 (see third row of Fig. B.19), there is no significant cor- 1867
 820 relation between the residuals. Moreover, in the “after” 868
 821 plots, there is almost no correlation between the residual 869
 822 in one sensor versus those in another, except in the tail 870
 823 of the distributions.

824 Appendix C. Validation through Simulations 873

825 To validate the alignment process, we followed the pro- 875
 826 cedure detailed in Sec. 5 on MC simulations produced us- 876
 827 ing the GEMC package [16], which is based on GEANT4 [17]. 877
 828 The cosmic rays were simulated as ~ 1 GeV muons, while 878
 829 the “field-off” tracks from the target were simulated as 0.479
 830 to 5 GeV protons with polar angle $35^\circ < \theta < 135^\circ$, and
 831 full azimuthal coverage.

832 We performed three types of tests with simulations.
 833 The first was to generate events with a misaligned geom-
 834 etry and to initialize the KAA with the nominal alignment
 835 parameters. For this type of test, we only misaligned a
 836 few parameters at a time. The second was to generate
 837 the events using the nominal alignment and to initialize
 838 the KAA using values other than the nominal ones. The
 839 advantage of the second method is that multiple tests us-
 840 ing different parameters could be performed for the same
 841 MC sample. The third method is a hybrid of the first
 842 two, which included some misaligned parameters at the
 843 generator level, and non-nominal values for other param-
 844 eters (we chose to use the survey values for these). Only
 845 the results from the third type of test are included in this
 846 work, as it encapsulates the challenges from the other two
 847 tests; the other two were used only in the early stages of
 848 development of the analysis framework.

849 The results with the third type of test are presented
 850 here in a similar format to Sec. 6. The distributions of the
 851 residuals for each detector type and also the track χ^2/dof
 852 are shown in Fig. C.20. The residual distributions are
 853 narrower in the simulations than in the data (see Fig. 8),
 854 which may be attributed to a mis-modeling of the reso-
 855 lution effects in the simulations. The estimates for the
 856 resolution effects in the simulations are based on an ideal
 857 version of the detectors, and can be adjusted to better
 858 match those of the real detectors.

859 We determined the mean and FWHMs of the resid-
 860 ual distributions for each module. These are shown in
 861 Fig. C.21. Finally, we show the residual distributions’
 862 means and FWHMs for the simulations as a function of
 863 the kinematics in Fig. C.22. No trend is observed in the
 864 means of the distributions, however, the FWHMs in the
 865 BMTZ and SVT are considerably smaller for tracks with

low d_0 (*i.e.*, the “field-off” configuration), than in tracks
 with large d_0 (*i.e.*, cosmics). The reason for this is that in
 the “field-off” configuration, the particles pass through the
 SVT and BMTZ detectors nearly perpendicular to the \hat{s}
 direction, and therefore there is typically only a single hit
 in a cluster. For the cosmic tracks, this is not necessarily
 the case, so there may be multiple hits in a given cluster,
 causing the resolution to be worse for such clusters.

Overall, the MC simulations validate that our imple-
 mentation of the algorithm works for the CLAS12 CVT.
 The FWHMs of the track-residual distributions are greatly
 reduced after the alignment (albeit to smaller values than
 those obtained in the data) and the average χ^2 is reduced
 to near unity.

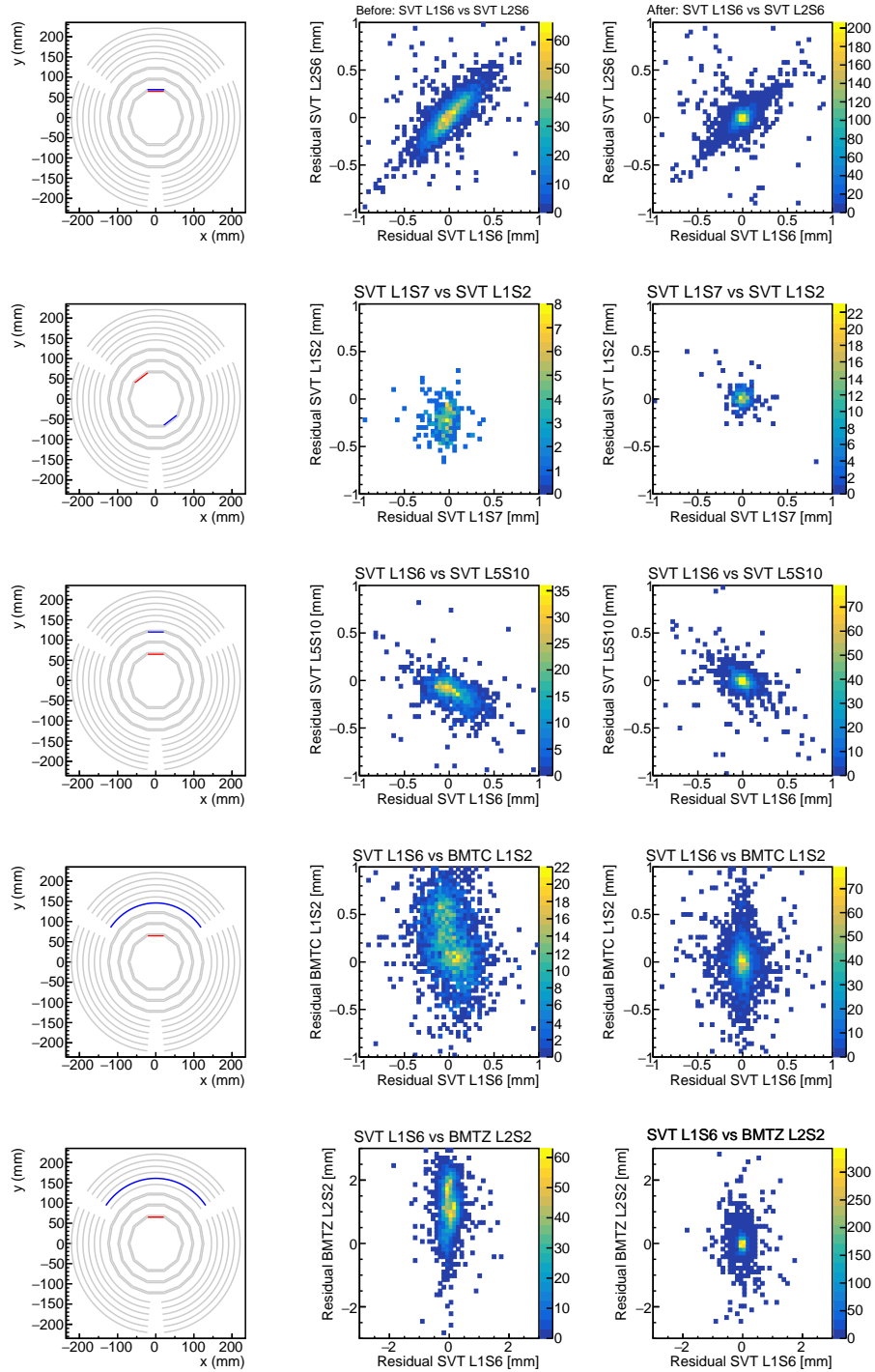


Figure B.18: Distributions of the residuals in one sensor versus those in another sensor within the same track before alignment (middle column) and after alignment (right column). For reference, the positions of the two sensors are shown to the right of the 2D residual plots. The combinations represent various topologies; from top to bottom, these represent: two SVT sensors in the same sector module, two SVT sensors in the same layer but azimuthally different sectors, two SVT sensors with overlapping sectors in different double-layers, an SVT sensor vs. an overlapping BMTZ sensor, and an SVT sensor vs. an overlapping BMTZ sensor.

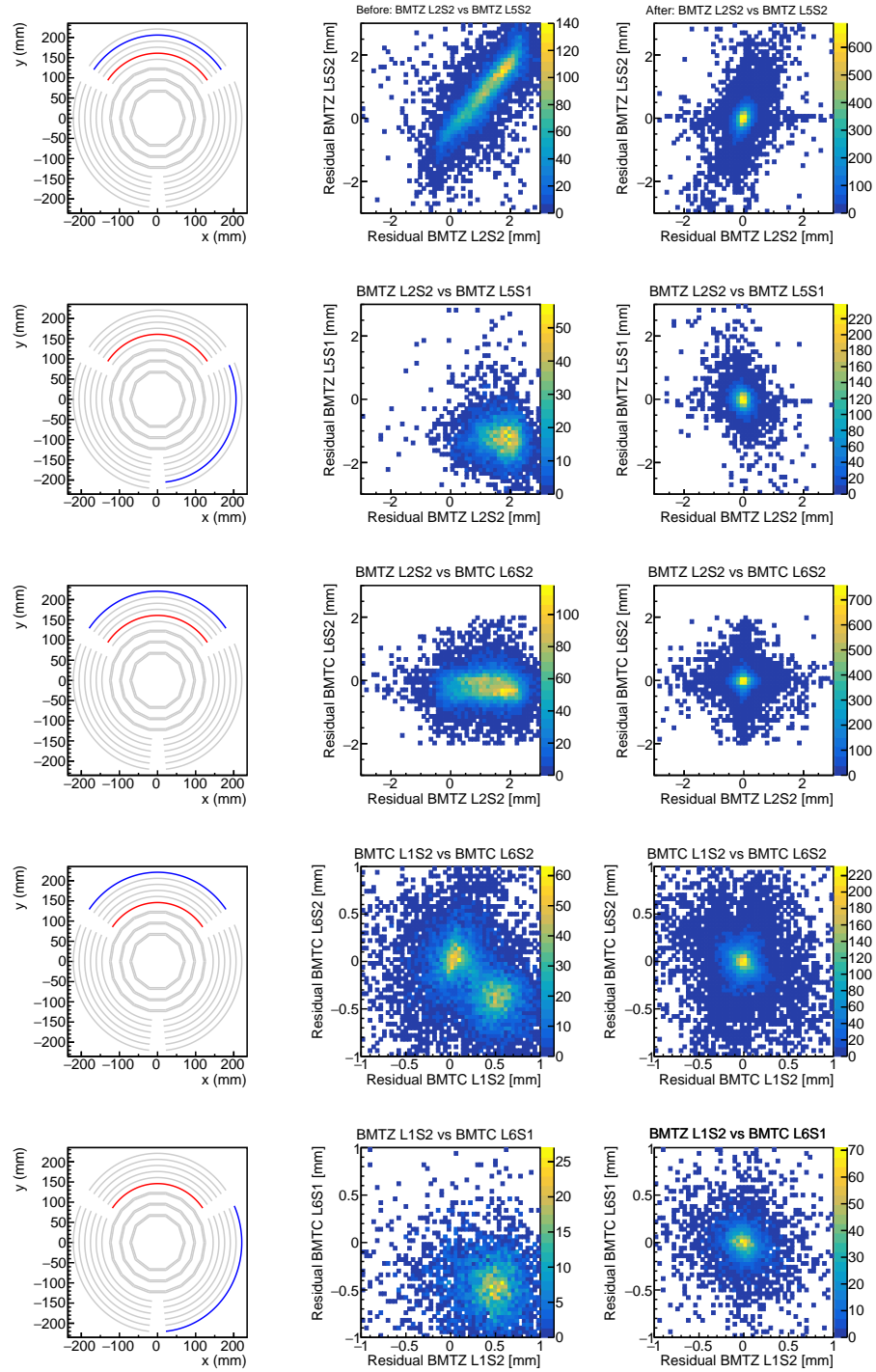


Figure B.19: Continued from Fig. B.18. From top to bottom, the topologies of the combinations shown are: two BMTZ sensors in the same sector but different layers, two BMTZ sensors in different layers and different sectors, a BMTZ sensor and a BMTZ sensor in different sectors and different layers, two BMTZ sensors in different layers but the same sector, and two BMTZ sensors that are in different sectors and different layers.

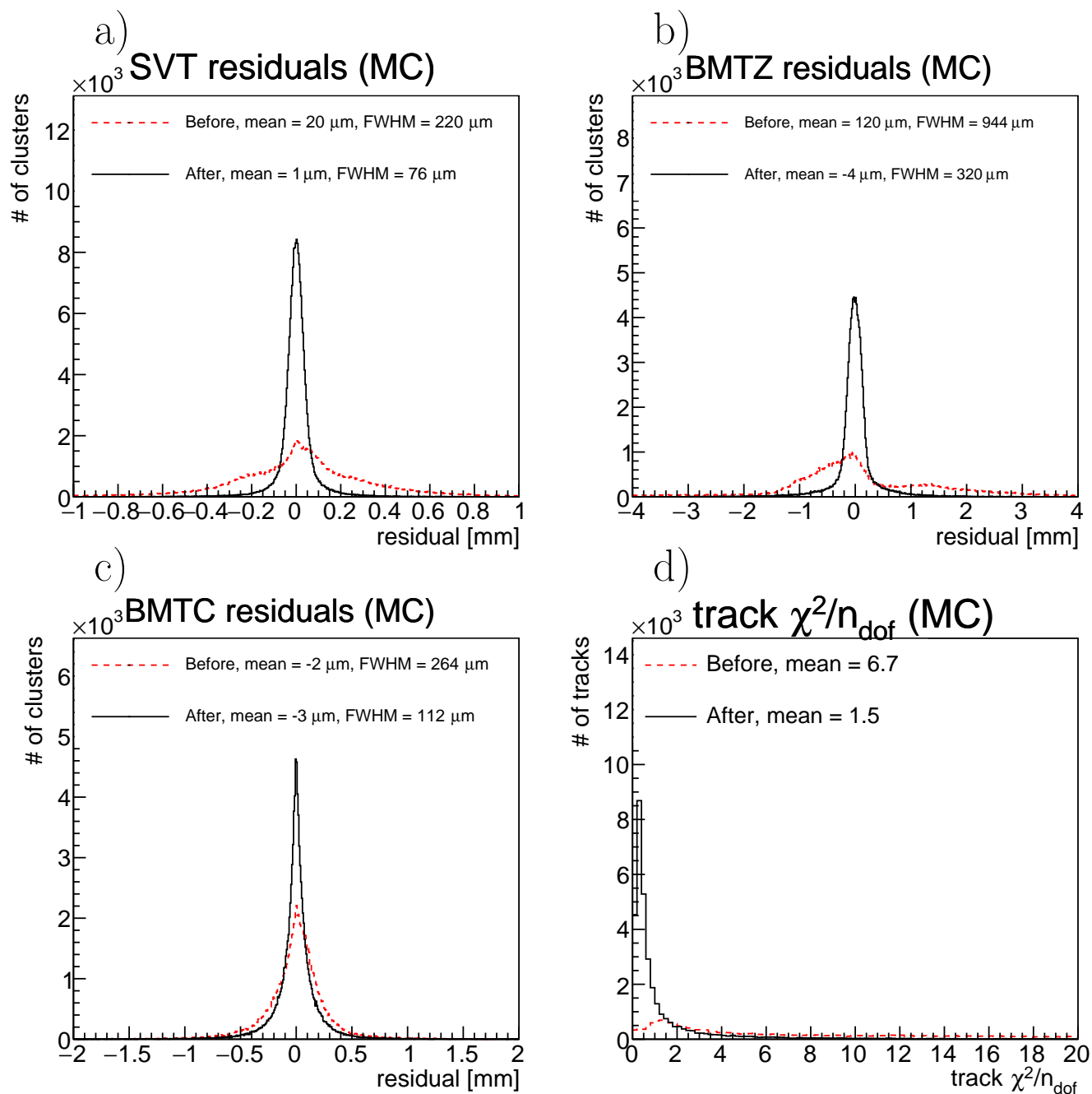


Figure C.20: Distributions of the residuals in the MC simulations before (red, dashed) and after (black, solid) alignment for the SVT (top left), BMTZ (top right) and BMTC (bottom left), and the χ^2/dof distribution (bottom right) for each reconstructed track. Each hit cluster produces a single residual in the track fit.

Residuals (all modules, MC)

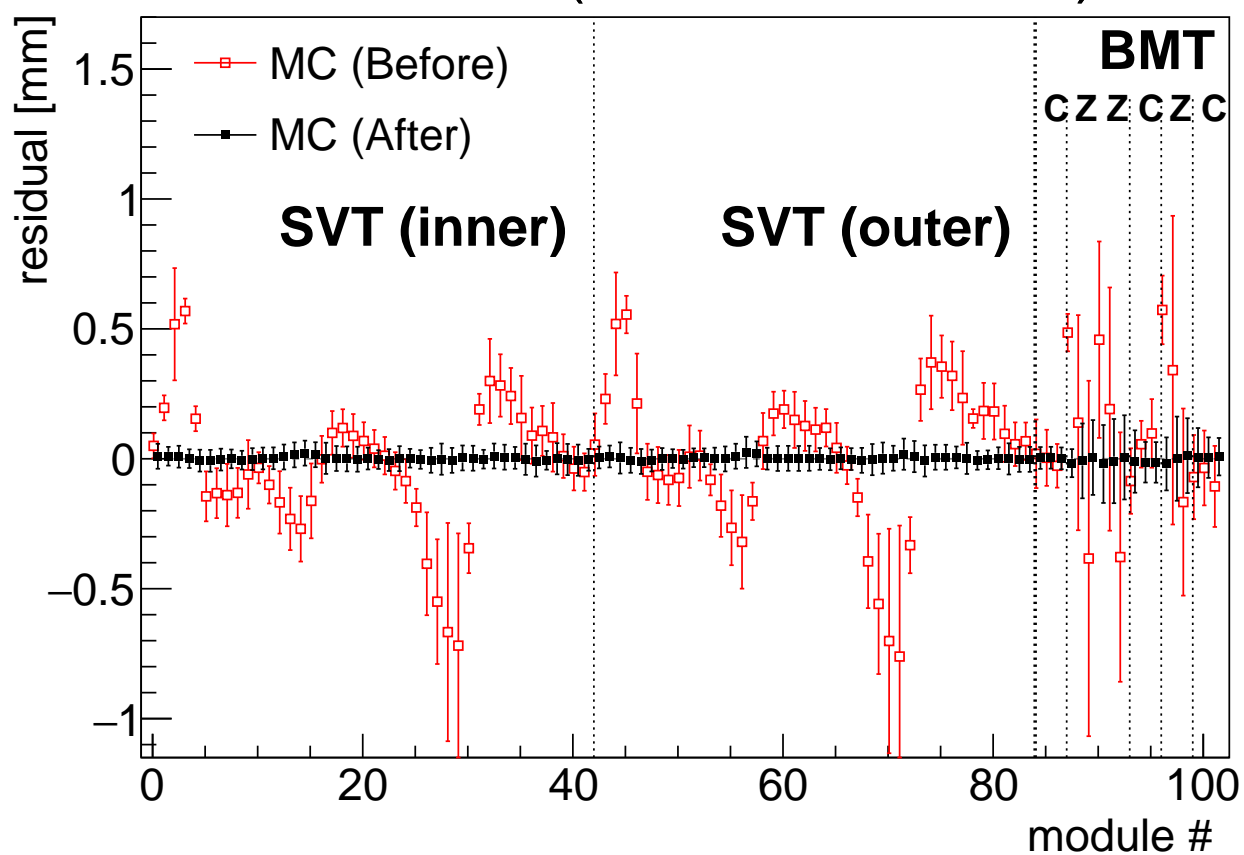


Figure C.21: Residuals in the MC simulations for the each module, before (red, open symbols) and after (black, closed symbols) alignment. The error bars for each point represent the FWHMs of the distributions, divided by two (so that the distance from the top of the upper error to the bottom of the lower error bar is one FWHM). Module numbers 1-84 represent SVT modules; numbers 85-102 represent BMT layers. Symbols are shifted horizontally slightly for clarity.

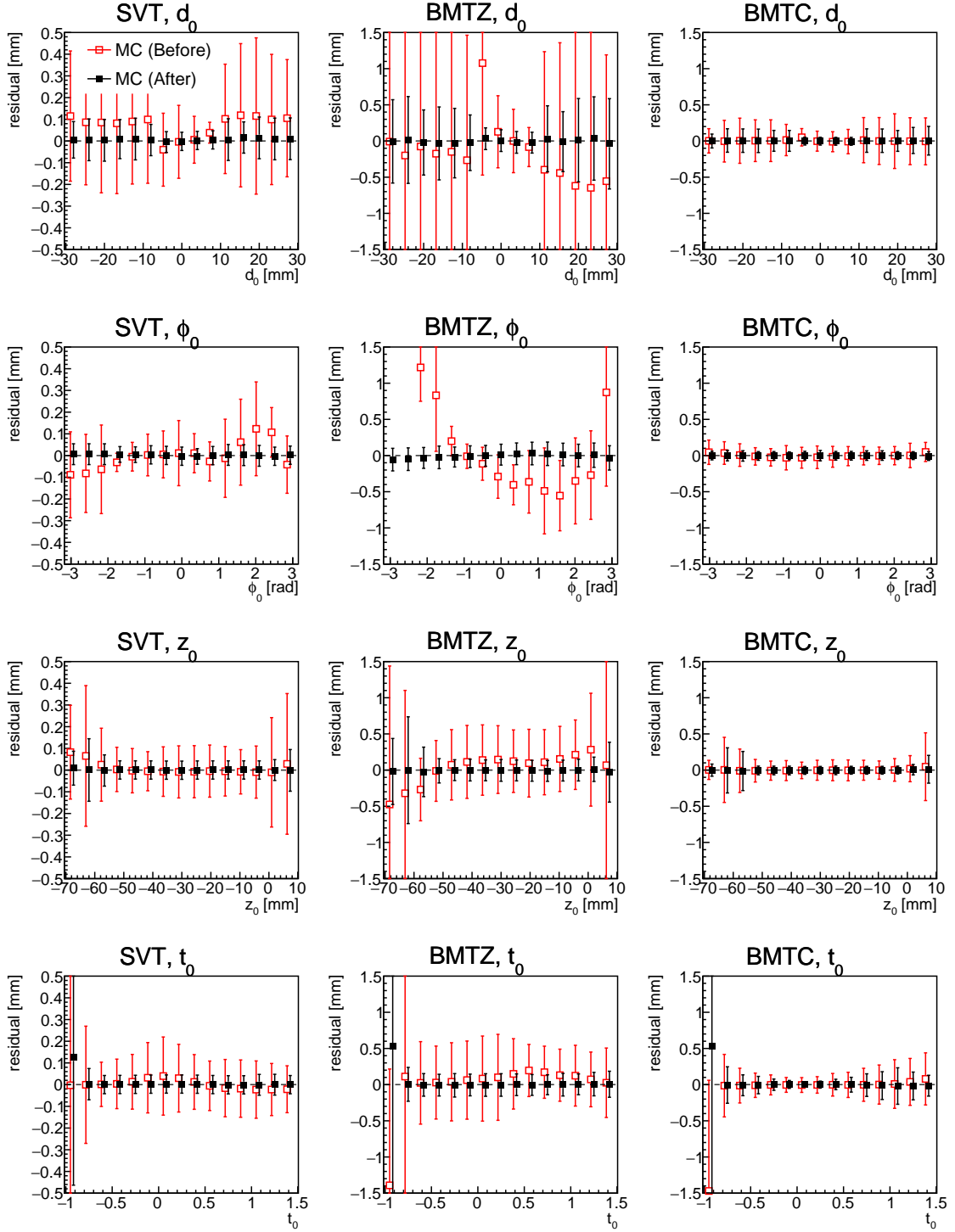


Figure C.22: Residuals in the MC simulations before (red, open symbols) and after (black, closed symbols) alignment, as a function of the kinematic variables: from top to bottom, d_0 , ϕ_0 , z_0 , and θ_0 . The error bars for each point represent the FWHMs of the distributions, divided by two (so that the distance from the top of the upper error to the bottom of the lower error bar is one FWHM). From left to right, the results are shown for the SVT, BMTZ, and BMTC. Symbols are shifted horizontally slightly for clarity. Note: Some of the “before” points are missing due to being outside of the range of the plot.